

PIERCING PHASE SIMULATION OF FLOW DRILL SCREWDRIVING®
(FDS®) FOR SHEET METAL JOINING

by

ROMANO ALOVISETTI

A Thesis submitted in partial fulfillment of the
requirements for the degree of

MASTER OF SCIENCE IN MECHANICAL ENGINEERING

2021

Oakland University
Rochester, Michigan

Thesis Advisory Committee:

Sayed A. Nassar, Ph.D., Chair
Giovanni Belingardi, Ph.D.
Zhijun J. Wu, Ph.D.
Lianxiang Yang, Ph.D.

© Copyright by Romano Aloviseti, 2021
All rights reserved

To my Mother and Father

ACKNOWLEDGMENTS

I want to express my gratefulness to Professor Nassar, whose teaching and efforts were fundamental for this work: his readiness at every hour, by day or by night, together with his detailed help on every possible difficulty, allowed me to successfully complete this experience in the US, even without moving from my house in Italy due to the World-spread pandemic.

A great thanks goes to Professors Belingardi and Cavatorta, who followed me during this whole experience, sustaining me with their knowledge and encouragement; together with Dr. Catelani, they were able to provide me a Simufact[®] Forming[®] license, without which this work would not have been possible.

I am grateful to MSC[®] Simufact[®] engineers of the customer support section, who satisfied all my requests: from simple questions regarding forwarding a completed simulation, up to complete model check and testing, even after my license was expired.

Last but not least, I must demonstrate here my deep gratitude to Dr. Pepe, my Stellantis[®] CRF[®] advisor: with him, many hours were spent in Google[®] Meet[®] to enhance and complete the required simulations, for a total of more than 200 runs within two (Summer!) months; even outside his working day and in the weekends, he was willing for advices, documentation, support for the software and for experimental testing: I finally learnt Flow Drill Screwdriving[®] thanks to him and to his great motivation and dedication to his work.

Romano Aloviseti

ABSTRACT

PIERCING PHASE SIMULATION OF FLOW DRILL SCREWDRIVING® (FDS®) FOR SHEET METAL JOINING

by

Romano Aloviseti

Adviser: Sayed A. Nassar, Ph.D.

In this Thesis research, the piercing phase of Flow Drill Screwdriving (FDS) for joining sheet metal is investigated. Starting from their main characteristics, as well as the process phases for their assembling, the author describes the Screws in their main parameters, then focuses on the steps required to correctly assembly them. Lately, the process parameters are analyzed, mainly axial force applied, torque and rotational speed, followed by the main defects. Consequently, the common applications are described, including the tests needed for reliability assessment. In the next section, the main physics behind these screws is reported, including a state of the art based on available documentation on precedent research and experiments, as well as the experimental set-up adopted for joint mechanical characterization and data on the workpiece material, AW6082-T6. Next, the 2D geometrical Axisymmetric model is defined within MSC® Simufact® Forming 2020 for the DP600 and AW6082-T6 piercing phase. Due to the drilling procedure, a careful description of the heat generation and flow is included into the FE model. These allow for the Scaling Factors choice to consider the temperature effect on the material properties.

Subsequently a Factorial analysis is developed to optimize all the most relevant factors both for the simulation and for the joint manufacturing process. In particular for what concerns the simulation factors, such as Coulomb μ friction coefficient, Interface shear factor m and screw rotational speed (rpm), variations on workpiece material, thickness and width, as well as on lower sheet-screw contact condition and FDS rotational speed, simulations are performed to observe the implied changes and, possibly, compare them with experimental evidence.

TABLE OF CONTENTS

| | |
|--|-----|
| ACKNOWLEDGMENTS | iv |
| ABSTRACT | v |
| LIST OF TABLES | ix |
| LIST OF FIGURES | x |
| LIST OF ABBREVIATIONS | xiv |
| | |
| CHAPTER ONE | |
| INTRODUCTION AND LITERATURE SURVEY | 1 |
| 1.1 FDS characterization | 3 |
| 1.2 Physics behind FDS | 14 |
| 1.3 Objectives | 24 |
| | |
| CHAPTER TWO | |
| METHODOLOGY | 25 |
| 2.1 Experimental set-up | 25 |
| 2.2 CAD and Numerical Model development | 34 |
| | |
| CHAPTER THREE | |
| RESULTS AND DISCUSSION | 44 |
| 3.1 Main factors influencing the simulations | 45 |
| 3.2 Model testing | 64 |

TABLE OF CONTENTS—Continued

| | |
|---|----|
| CHAPTER FOUR CONCLUSION | 82 |
| CHAPTER FIVE SUGGESTED CONTINUATION WORK | 84 |
| REFERENCES | 87 |

LIST OF TABLES

| | | |
|----------|---|----|
| Table 1 | Coefficients employed in Eq 2. | 18 |
| Table 2 | Coefficients used in Eq 3. | 18 |
| Table 3 | The combined Stick-Slip contact condition. | 21 |
| Table 4 | Main properties of the materials employed. | 25 |
| Table 5 | The experimental tests' input parameters. | 27 |
| Table 6 | J-C Model Parameters for AW6082-T6. | 32 |
| Table 7 | Coefficients for Young Modulus - temperature fitting polynomial for AW6082-T6. | 32 |
| Table 8 | FEA Simulations' required acceptance criteria. | 40 |
| Table 9 | Factorial analysis' factors. | 41 |
| Table 10 | Combination for each Factorial analysis' run. | 55 |
| Table 11 | Summary of factors' effect on each output. | 61 |
| Table 12 | Friction Laws and coefficients combination of the tribological analysis. | 70 |
| Table 13 | Important workpiece quotes: Combined Stick-Slip vs. Mixed Coul-Shear vs. average experimental evidence. | 72 |

LIST OF FIGURES

| | | |
|-----------|---|----|
| Figure 1 | The EJOT EXTERNAL TORX PLUS [®] , M5x25. | 4 |
| Figure 2 | Tool used in Friction Drilling. | 5 |
| Figure 3 | WLC [®] TAPTITE [®] , common Thread Forming screw, [4]. | 6 |
| Figure 4 | The Flow Drill Screwdriving phases, [5]. | 7 |
| Figure 5 | The WEBER RSF21 machine, [12]. | 9 |
| Figure 6 | The assembling machine' parameters. | 10 |
| Figure 7 | Example of successful assembly. | 11 |
| Figure 8 | FDS joint: Two simple sheets (a) and with pre-drilled hole (b). | 13 |
| Figure 9 | Characteristic Time vs. Torque curve. | 15 |
| Figure 10 | Functional sections of the EJOT EXTERNAL TORX PLUS, M5x25. | 19 |
| Figure 11 | The experimental apparatus (a) and specimen (b). | 26 |
| Figure 12 | Macrography of P44 - successful piercing test. | 28 |
| Figure 13 | Macrography of P43 - unsuccessful piercing test. | 28 |
| Figure 14 | Thermocouples position (a) and macrography (b). | 29 |
| Figure 15 | The Temperature-Time curve of test P34, at radial distance of 10mm. | 30 |
| Figure 16 | Young' Modulus of AW6082-T6 <i>versus</i> temperature. | 33 |

LIST OF FIGURES—Continued

| | | |
|-----------|--|----|
| Figure 17 | $\sigma - \varepsilon$ curves at different temperatures for AW6082-T6. | 34 |
| Figure 18 | Friction Welding module' main settings. | 35 |
| Figure 19 | Adopted Coulomb' μ - temperature relation. | 37 |
| Figure 20 | Section of the modeled assembly. | 39 |
| Figure 21 | L1 and L2 geometrical meaning. | 42 |
| Figure 22 | Heatmap for Scaling Factors at 0°C and Melting Point. | 45 |
| Figure 23 | Lower extrusion detachment (a) and chip formation (b). | 47 |
| Figure 24 | Self-intrusion at upper extrusion (a) and at contact surface with screw (b). | 48 |
| Figure 25 | Experimental vs FEA extrusions, geometrical comparison. | 49 |
| Figure 26 | FEA <i>versus</i> experimental End Load. | 51 |
| Figure 27 | FEA <i>versus</i> experimental temperature. | 51 |
| Figure 28 | Standard vs. expanded specimen' FEA temperature. | 53 |
| Figure 29 | Equivalent Stress distribution in the FEA workpiece. | 54 |
| Figure 30 | Main Effect Plot and Pareto Chart for <i>Perc</i> response. | 56 |
| Figure 31 | Main Effect Plot and Pareto Chart for <i>L1</i> response. . | 58 |
| Figure 32 | Main Effect Plot and Pareto Chart for <i>L2</i> response. . | 60 |

LIST OF FIGURES—Continued

| | | |
|-----------|---|----|
| Figure 33 | Response Optimization for <i>Perc</i> , <i>L1</i> and <i>L2</i> . . | 62 |
| Figure 34 | Deformable (a) vs. rigid (b) screw: FEA geometrical and thermal comparison at lower sheet. | 65 |
| Figure 35 | Deformable (a) vs. rigid (b) screw: FEA geometrical and thermal comparison at screw. | 66 |
| Figure 36 | Deformable vs. rigid screw: exerted End Load from FEA. | 67 |
| Figure 37 | Without (a) and with (b) damage criterion: FEA geometrical and thermal comparison at lower sheet. | 68 |
| Figure 38 | Without (a) and with (b) damage criterion: effect on lower sheet' extrusion in FEA model. | 69 |
| Figure 39 | Combined Stick-Slip (a) vs. Mixed Coul-Shear (b): FEA geometrical and thermal comparison of extrusions. | 71 |
| Figure 40 | F_z in FEA, Combined Stick-Slip (a) vs. Mixed Coul-Shear (b). | 73 |
| Figure 41 | Combined Stick-Slip (a) vs. Coulomb only (b): FEA geometrical and thermal comparison of extrusions. | 74 |
| Figure 42 | Combined Stick-Slip (a) vs. Shear only (b): FEA geometrical and thermal comparison of extrusions. | 75 |
| Figure 43 | AW6082-T6 (a) vs. AW6061-T6 (b): FEA geometrical and thermal comparison of extrusions. | 76 |
| Figure 44 | The AW6061-T6 case End Load graph from FEA. | 77 |
| Figure 45 | 2.0mm thick (a) vs. 3.0mm thick (b): FEA geometrical and thermal comparison of extrusions. | 78 |

LIST OF FIGURES—Continued

| | | |
|-----------|--|----|
| Figure 46 | 8000 rpm (a) vs. 5000 rpm (b): FEA geometrical and thermal comparison of extrusions. | 80 |
| Figure 47 | 8000 rpm (a) vs. 6000 rpm (b): FEA geometrical and thermal comparison of extrusions. | 80 |
| Figure 48 | An example of valid Lower Sheet mesh. | 83 |
| Figure 49 | Thread ripping in 3D numerical simulations. | 85 |

LIST OF ABBREVIATIONS

| | |
|------------|---|
| K | Nut Factor |
| D | Nominal bolt diameter, [mm] |
| A_t | Bolt tensile area, [mm ²] |
| p | Bolt pitch, [mm] |
| d_t | Effective thread contact diameter, [mm] |
| d_{min} | Notch diameter, [mm] |
| μ_t | Thread friction coefficient |
| μ_b | Underhead bearing friction coefficient |
| σ_u | Ultimate Strength, [MPa] |
| E | Young' Modulus, [MPa] |
| S | Engineering Stress, [MPa] |
| e | Engineering Strain |
| T_{room} | Room Temperature, [°C] |
| T_{melt} | Material Melting Temperature, [°C] |

CHAPTER ONE

INTRODUCTION AND LITERATURE SURVEY

In accordance with the increasing interest for the environment and against the global warming phenomena, the reduction of noxious pollution, in particular of the Greenhouse Gases such as the CO₂, due to road vehicles is strictly related to the vehicle weight: the higher is the mass, the higher will be the fuel consumption, so that lightweight of vehicles is one of the main goals for which new technologies in the Automotive field are developed.

In order to reduce weight, a successful solution is to adopt materials lighter than Steel for as many parts as possible: the limit lays in the necessity for confidence on structural characteristics that, as a matter of more than one century and half of use, only Steel has, as well as in the overall cost for the final product. In this field, Aluminum and its alloys are arising many interests, considering their mechanical properties compared to low density and moderate price. A number of multi-material (also called hybrid material) solutions have been developed to take advantage from the particular properties of each. At this point, the main difficulty is joining Steel stiffening parts to Aluminum frames: it is well known that Resistance Spot Welding, widely used for full steel structures, cannot be considered for multi-material structures, so that adhesive bonding or brazing are adopted [1]. Adhesive bonding is also employed in vehicle' weight reduction since High Strength Steels (HSS) and Ultra High Strength Steels (UHSS) present some difficulties at welding [2]. In these cases (including the multi-material cases) another joining technique, the *Flow Drill Screwdriving*[®] (FDS[®]), has recently gained interest. It was at first

documented around the year 2014 by Ford and General Motors [3], it has seen a widespread development among many Carmakers for its reliability and easiness of use compared to moderate price.

The main advantages, part of which exposed by the manufacturer EJOT[®] [4], are:

- Possibility to join different materials.
- High mechanical resistance to traction and shear loads.
- High reliability of the “added part” (the screw, made of case-hardening Steel, Zinc coated).
- Absence of material removing, as well as surface treatments required.
- Pre-drilled hole for the upper sheet is not usually needed (although sometimes adopted to improve the joint feasibility).
- Possibility for joint disassembling, in a recyclability context.

One main disadvantage is the process characterization, whose physics requires a deepened analysis on its phases and parameters for the evaluation of applicability in the Process Development phase. In this field, the most complete research was performed by Skovron [6] as reported in his Ph.D. dissertation, where he presented the screws’ characteristics, the process insight, the industrial techniques having aspects in common with it and further optimization steps. What is missing is the possibility to easily adapt his research’ analytical results to the FEA Simulations, so that to verify feasibility of this joining technique via a straight-forward procedure.

Regarding the FDS process parameters, Aslan et al. [7] performed two analyses: the former, centered on drilling tests of an AW5182-O Aluminum layer, by varying the

screw' rotational speed and the axial force applied by the assembling machine and its blank holder on the workpiece, the latter, focused on FDS single-lap joint characterization, by evaluating the variation of its mechanical properties (the author concentrated his attention on the Maximum Cross Tensile Force allowable before failure) for four different sets of parameters, two of which affected each by a possible process defect. The most interesting result, apart from the determination of the relationship among parameters and consequent defects, is the absence of defects-related drawbacks in Quasi-static conditions, although this is not ensured for dynamic loads (i.e., fatigue), which are commonly encountered in the vehicle utilization.

Concerning FEA Simulation, great efforts were done by Pan et al. [8], who adapted a recent stabilization algorithm (the Momentum-Consistent Smoothed Particle Galerkin Method), based on a Mesh-free system, to solve the issues relative to the high deformation of the element's mesh due to Friction Drilling, which led to simulation failures and increased Computational Time. Afterwards, Wu et al. [9] exploited the stabilization algorithm on FDS thread forming simulation, for single sheet only, with interesting results. Even accepting the complexity in applying this Mesh-free approach to Numerical Simulations, these works are not centered on the screw' physical aspects, so that the analyses they performed could lead to possible defects, and even failures, in the reality.

1.1 FDS Characterization

In order to understand the overall Flow Drill Screwdriving technique, the first step implies analyzing the screw itself, as it is presented in Figure 1.

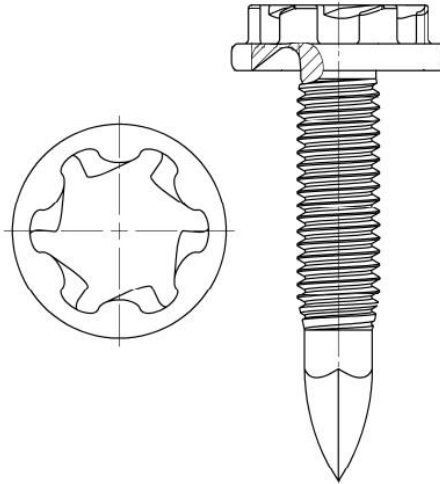


Figure 1. The EJOT[®] EXTERNAL TORX PLUS[®], M5x25.

The principal aspect standing out is its shape:

- The tip is four-lobed, without any thread and ending in a cylindrical zone.
- The passage from the tip to the standard threads is gradually obtained via a conical-shaped threaded section.
- The shank, reduced to the minimum, is employed to guide the outflowing material in the cavity behind the screw' head, peculiarly designed for the purpose.

What greatly differentiates screw' models among them is the head, whose profile and dimensions have been developed for automated assembling, disassembling safety reasons and best deformation resistance to applied torque.

The shape in which the Flow Drill Screw is governed by two different industrial aspects of the joining process that it performs: Friction Drilling and Thread Forming.

Friction Drilling [10] is adopted to perforate metal sheets/tubes without material removal. As the name says, it is based on the relative friction between the rotating tool,

schematized in Figure 2, and the workpiece: friction causes a relevant rise of the local temperature of the latter' material up to its melting point, the tool penetrates, then its shoulder presses the outflown metal, deforming it into a boss.

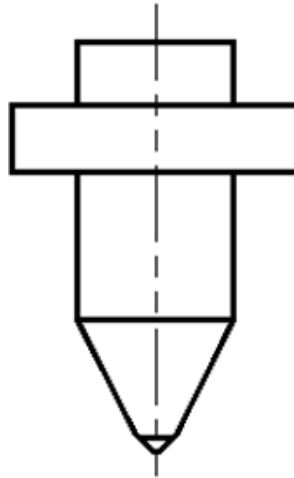


Figure 2. Tool used in Friction Drilling.

In common with FDS process, the tool' tip is optimized to enhance the friction effect, thanks to its large contact surface, including that there is no lubrication. On the other hand, FD tool is typically made in Tungsten-Carbide alloy and, since the workpiece materials are much "softer", it is used for drilling many holes before it reaches the conditions for being substituted. This results in having a temperature at process start higher than room' (and so, screw') as well. Moreover, as one of the main differences between the two types of process, FDS tips are lobed to rapidly penetrate the material, while FD' ones are smooth conical.

Thread Forming [11] is a common process in the mechanical industry; in this case, the action is performed by a peculiarly-designed screw rather than a tool (Figure 3). It differentiates from Self Cutting screws mainly for the dimensions of the threads, intended to deform the workpiece material rather than removing it, to obtain grain refinement and subsequent stiffer female threads.

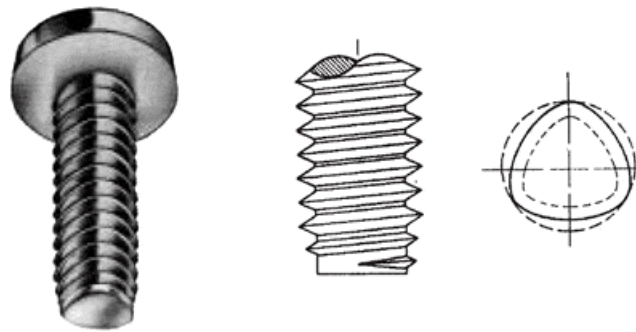


Figure 3. WLC[®] TAPTITE[®], common Thread Forming screw, [4].

With respect to Flow Drill Screws, Thread Forming ones are fully threaded, preferably three-lobed, and require a pre-drilled hole to be assembled. This fact increases the overall Process Time and costs. Moreover, in Thread Forming there is no material overflowing from the hole, thus those screws do not have heads studied for the purpose. On the other hand, these two kinds of screws have similar thread profiles and are made of similar alloys, although Zinc coating for TF ones is not required.

Going on with the FDS process, after the Thread Forming step, the Screw Driving and Tightening phases are executed: the machine itself monitors and recognizes when the

preset stopping values of the control parameters are reached, so that to avoid issues affecting the just formed threads like thread ripping.

Now, it is time to present the complete Flow Drill Screwdriving technique (Figure 4).

As said before, it can be mainly divided into these subsequent phases:

- Piercing (or Hole Drilling).
- Thread Forming.
- Screw Driving and Tightening.



Figure 4. The Flow Drill Screwdriving phases, [5].

It must be pointed out that, as in Friction Drilling, material melting temperature is not reached, and the high temperatures generated close to the rotating screw lead to ductile deformation, with gradual grain size elongation, useful for the successive Thread Forming phase (as studied in [6]).

In Figure 4, you can also notice that the outflown material is fundamental for the correct joining, since most threads are formed in this section: peculiarly, the metal pushed by the

screw generates the *extrusion* (which is completely threaded), while the quantity displaced over the upper sheet is shaped into a *boss*, which is partially threaded, increasing the underhead Contact Surface (for loosening resistance).

To better understand how FDS is possible, the assembling apparatus must be investigated. As evident from Figure 5, the process is automated, performed by robots due to the important weight of the machine (approx. 50 kg, [12]); in the call-out, the tool' black C-shaped appendix is the Blank-holder, first contacting the sheet, then the screw is posed in rotation via the metallic cylinder and pressed by the hydraulic system on the surface, initially kept in position by jaws. All the procedure is simultaneously monitored in terms of screw rotational speed and applied axial force , as well as vertical positioning of the lower end of the screw' head with respect to the upper workpiece's surface.

By comparing the time elapsed from the screw/sheet first contact with the vertical position, the *Depth Gradient* is computed, which is useful to check the correct penetration of the screw in each phase. The *Applied Torque* monitoring is fundamental in Screw Driving and Tightening: in particular, the contact between screw' head and upper sheet constitutes the checkpoint between these two actions, at which the rotational speed must be dropped.

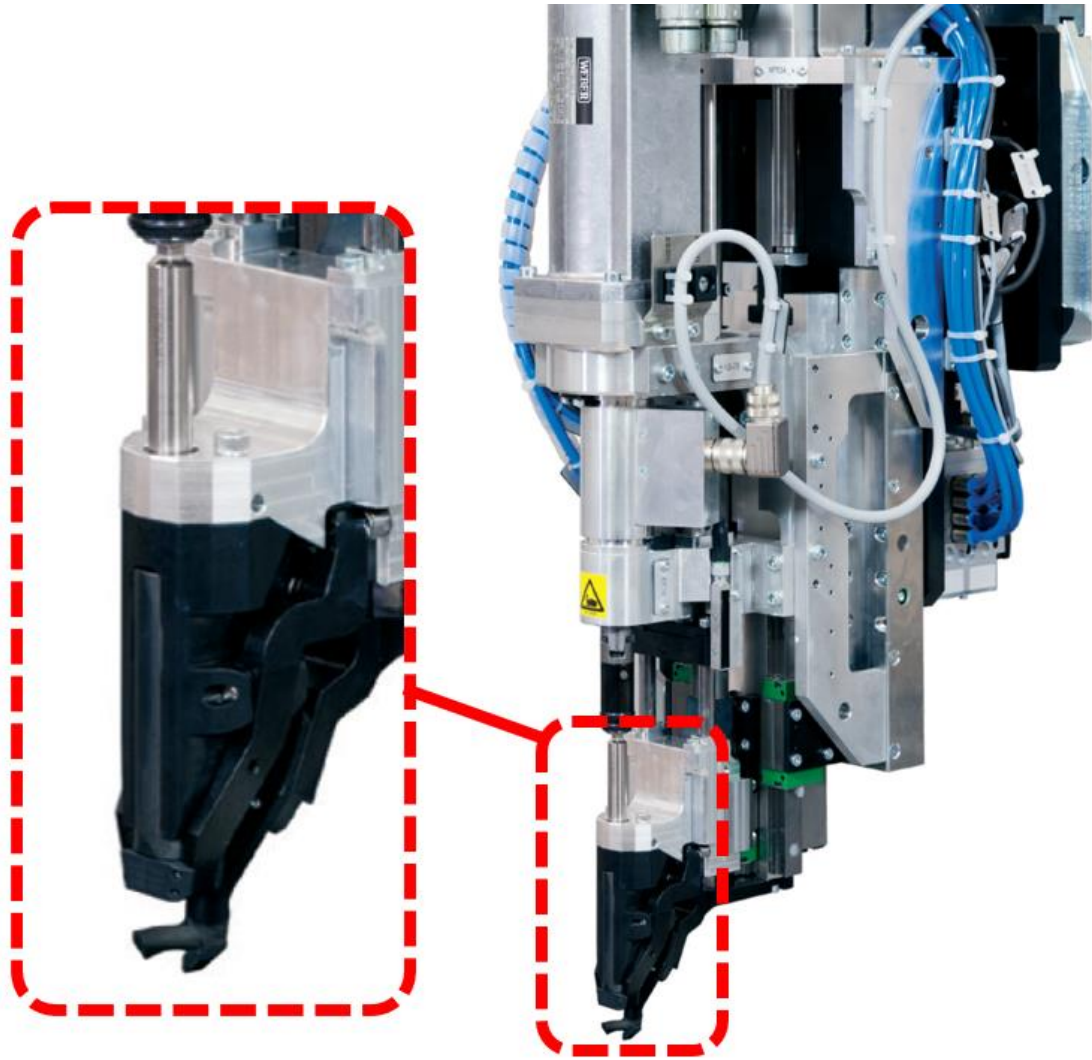


Figure 5. The WEBER® RSF21 machine, [12].

To ensure the optimization in terms of time, the *Ramp Time* is fixed: it is the maximum period the machine has to adapt a given process parameter (rotational speed and/or axial force) to a target value, stated for each phase.

In Figure 6, the assembling machine's parameters are described: it results that the phases for the machine control partially differ from the ones pointed out in Figure 4.

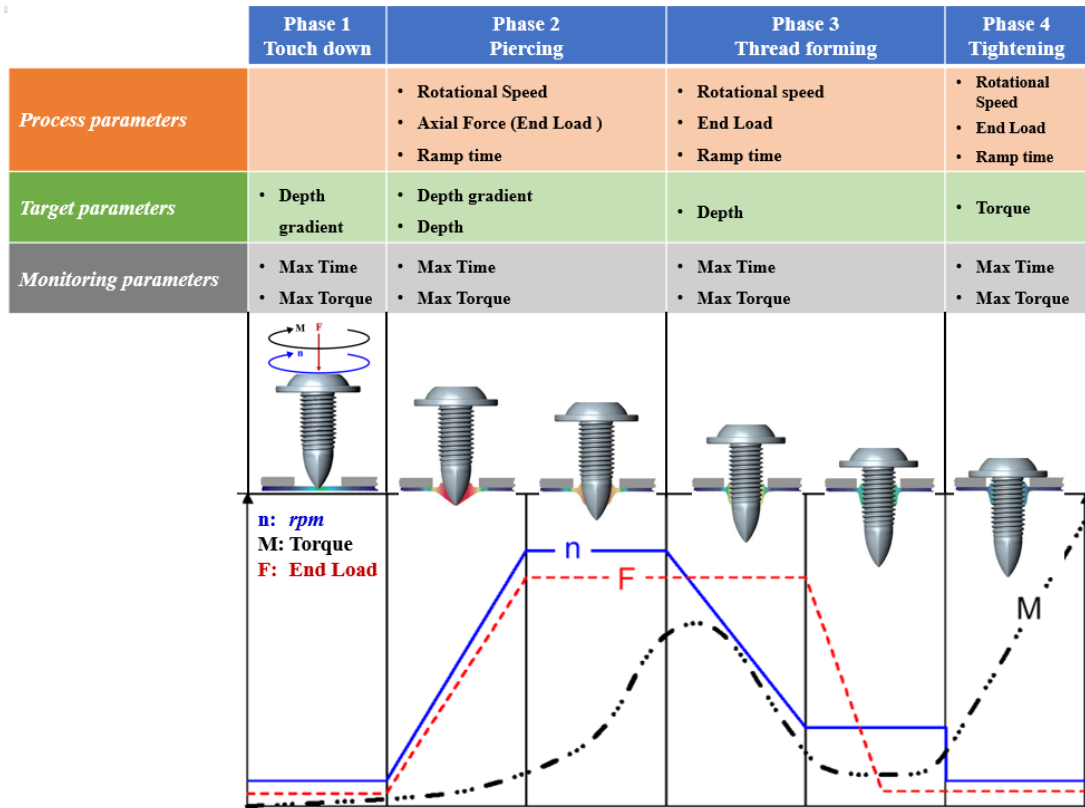


Figure 6. The assembling machine' parameters.

It can be noticed that rotational speed and axial force have been sketched as straight lines, while the torque is drawn as a curve: this comes from the fact that the formers are Process parameters, to which the machine has to adequate the real resulting values, while the latter is a Monitoring parameter (as time elapsed), limited only at its maximum.

Now a question arise: when the assembling of a Flow Drill Screw is considered as “successful”? As far it is reported in the literature and in the industrial practice, it is mainly a geometrical aspect (Figure 7): the gap existing between the upper and the lower workpieces, due to the material flown in-between, must end within an imaginary cylindrical surface, containing the screw' head contour, and parallel to the screw' axis.

In this way, possible water and dirt infiltrations between the sheets are avoided, and the joint assembly does not significantly influence the surrounding sheet geometry.

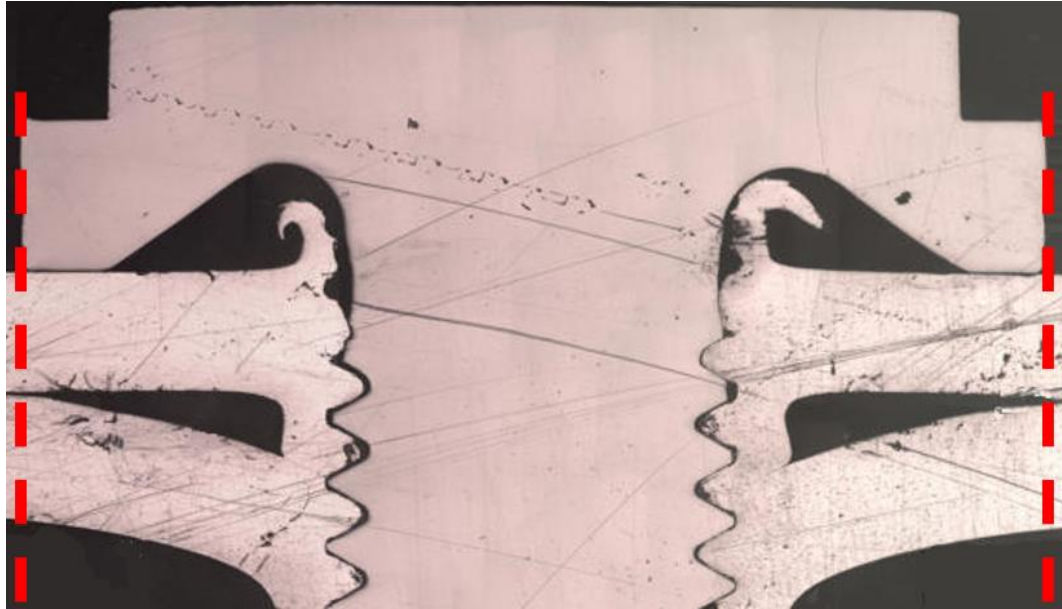


Figure 7. Example of a successful assembly.

Since such a verification cannot be performed for every joint, as it asks for the sectioning of the assembly, the Target parameters are crucial: when they are met, the machine automatically classifies the assembling as “successful”, so that to proceed to the following one. Referring to Piercing, some defects could arise [7], namely:

- *Chip Formation*, determining material removal and possible indentation of the chip under the screw’ head. As will be seen in the following, this type of defect is

mainly caused by material adhesion to the screw' tip, for high rotational speed and low axial force.

- *Bushing Fracture*, causing not-complete thread forming in it and workpiece local deformation. As will be seen in the following, this type of defect is consequence of high fastener force compared to mid-to-low rotational speed.

Screw failure must not be regarded as a possible defect of the FDS joining, since it is only met when overcoming the screw' Yield Strength, that is a case practically possible only in presence of service loads.

Flow Drill Screwdriving is performed with two plain workpieces, whose materials are usually softer than the screw', or to join pre-drilled harder upper sheet to softer, not-drilled lower one (Figure 8).

Some common applications are reported in high-end sportscars (ex. Audi R8, TT and A8, [5]), as well as in big vehicles (ex. Ford F150, [3]), mainly in the space-frame to join box structures or panels to the platform, with the well-known intent of weight reduction and reliable and stiff joint.

In order to verify the reliability of FDS assembly, the tests performed are:

- *Static Coach-Peel*, to evaluate the joint strength under combined tensile-shear loading; two L-shaped sheets are clamped in their shorter end with FDS, then tensile loads are applied at their longer end.
- *Lap Shear*; although designed to test only for shear loads, its results are like Peel test' due to the final deformation of the low stiffness workpiece; it can be done with two or three layers (i.e., overlapping sheets).
- *Dynamic Lap Shear*, with cyclic shear loads to test the joint under fatigue.

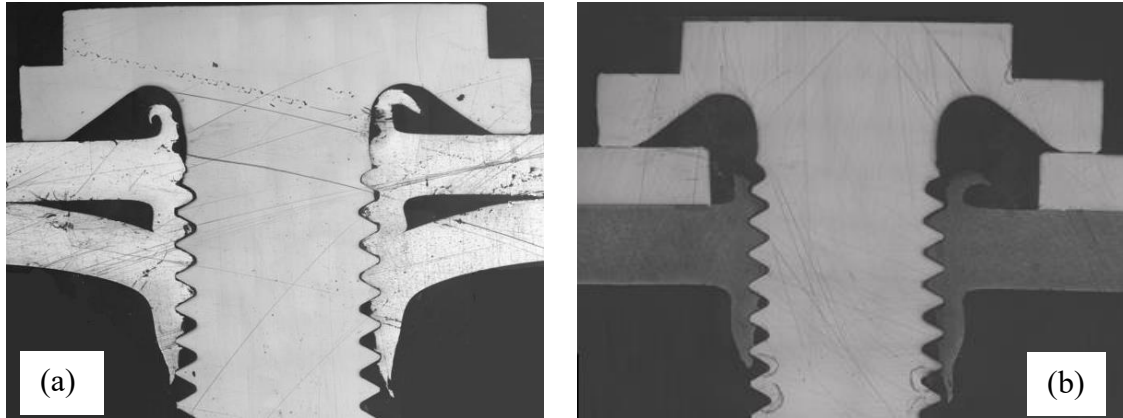


Figure 8. FDS joint: Two simple sheets (a) and with pre-drilled hole (b).

The possible failures associated to these experimental tests are strongly linked to the materials adopted: in case of both sheets having lower stiffness compared to the screw's, *screw pull-out* verifies; when the upper workpiece strength is lower than both the lower and the screw', *sheet tear-out* happens; *screw fracture* is evidenced only when its stiffness is lower than the sheets'. In dynamic loading conditions, it can result the cracking of the entire joint, starting from its threaded part.

Finally, other possible failures are related to the environment in which the screw will be adopted: considering the sheet assembly been usually constituted by High Strength Steel and Aluminum alloys, the Electrochemical compatibility plays an important role.

Due to this phenomenon, the Al sheet would encounter corrosion when an electrolyte bridges it to the Steel sheet. As the complete "sealing" of the inner region between the two sheets is a key point of FDS successful assembling, the presence of water, vapor and any other substance as electrolyte is not possible; to further prevent corrosion, adhesive

can be posed between the sheets, carefully avoiding the pre-hole region not to fill the just formed threads.

Regarding the screw itself, the Zinc coating is used as sacrificial anode, so that its HSS “core” is not deteriorated. Common tests in this field employ salt spray exposition for a period and temperature dictated by ISO 9227 and ASTM B117 standards.

1.2 Physics behind FDS

In order to understand the main physical laws behind this industrial technique, it is important to start from the principal characteristic relation: the Time vs. Torque curve, whose trend is similar to that presented in Figure 9 from experimental data. This graph is usually machine determined, i.e., the assembling machine has its own dynamometer which measures the *Torque Gradient*, intended as ratio between applied torque and measurement time interval, and then converts it into the Time vs. Torque relation. These data are used to monitor the process. Data filtering is a common practice adopted in post-process analysis in order to minimize the effect of external factors (generally referred to as “noise”) which could influence the torque evaluation, especially considering the high peaks registered in a limited amount of time (up to 3000 Nm/s during Tightening).

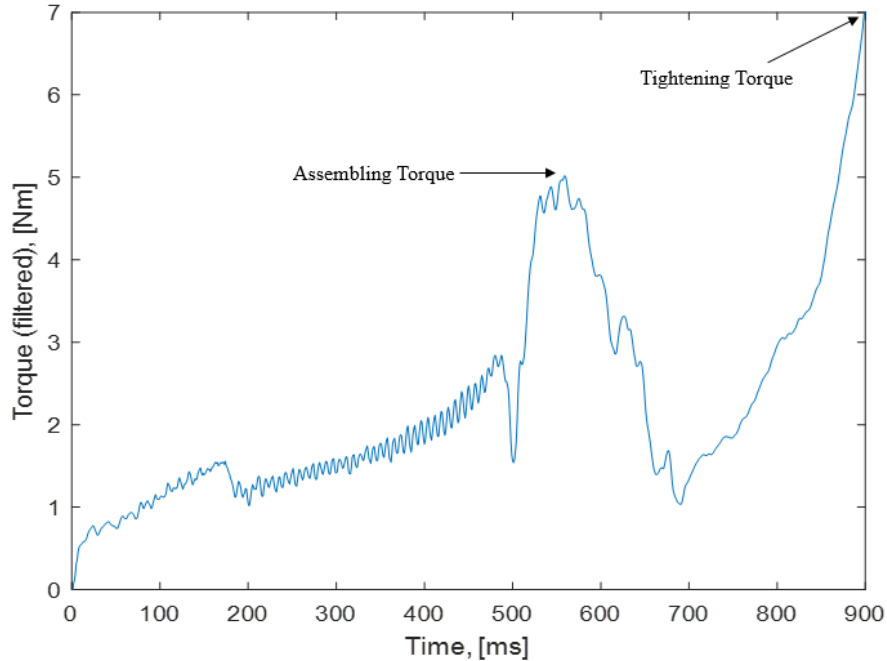


Figure 9. Characteristic Time vs. Torque curve.

From Figure 9, you can retrieve the main steps of the process:

- Starting from time = 0 ms, up to close to 500 ms, torque increases due to the screw' tip pushed on the workpiece, and, thanks to the relative friction, the contact point is heated up, so that the material reaches the plasticity condition necessary for the screw penetration.
- The subsequent steep torque falling-arising is caused by thread forming, from the moment in which the cylindrical portion of the screw slides into the material due to the low relative friction induced by high local temperatures, to the screw's threads shaping the surrounding metal into female threads, up to reaching the *Assembling Torque* and always without material removal.

- Torque reduction because of screw driving into the fully threaded workpiece, consequently a growth at first due to the sheet metal deforming around and under the screw' head into the boss, then generated by the tightening phase, up to the designed value for screw preload (defined as *Tightening Torque*).

From this description, some useful parameters come out, necessary for the correct design of the technique; they are:

- *Assembling (or Driving) Torque*, the most critical value in determining joint feasibility. Its limiting value comes from the maximum shear stress of the FDS. Thicker plates/stronger materials require higher torque for thread forming, with the help that material strength is negatively affected by the rise in temperature due to frictional heat generation.
- *Stripping Torque* (rounded to the *Tightening Torque*). In tightening to the highest Clamp Load F , it is required not to overcome the material strength of the newly-created female threads, by limiting the torque at the Stripping Torque M_s , which is presented in [13].

$$M_s = \frac{KD\sigma_u}{\frac{1}{2A_t} + \sqrt{\left(\frac{1}{2A_t}\right)^2 + \left[\frac{16(0.16p+0.58d_t\mu_t)}{\pi d_{min}^3}\right]^2}} \quad (1)$$

where K is the Nut Factor, D is the nominal bolt diameter in [mm], A_t is the bolt tensile area in [mm²], p is the bolt pitch in [mm], d_t and d_{min} are respectively the effective thread contact and the notch diameter, in [mm], μ_t is the thread friction coefficient and σ_u is the Ultimate Strength of the screw' material, in [MPa].

- *Process Time.* Considering that this technique aims to replace Spot Welding, whose process time can be less than 0.6 seconds (per spot), time is certainly an important factor to consider and optimize. Most of the FDS Process Time is required in the hole drilling phase. To shorten it, you cannot exceed a limit in increasing the axial force that pushes the screw, since too high End Load could lead those defects already exposed.
- *Breakloose Torque.* Taking into consideration that joints will be exposed to high vibrational environments, that, as it is well known, is the main cause of self-loosening, the FDS self-loosening performance has to be measured in terms of their Breakloose Torque. One beneficial influencing factor is the Torque Holding Time: holding the screw at the Tightening Torque for a designated time can lead to an increased Breakloose Torque. Although increasing the total process time, the Breakloose Torque would benefit of a 15% rise for only an additional 0.5 s.
- *Maximum Temperature.* As friction induces local temperature growth in the workpieces, it must be noted that material melting is never reached (and it has not to be encountered): monitoring the Maximum Temperature is thus fundamental.

In order to determine these quantities, some inputs are required, namely rotational speed, End Load and Ramp Time, as well as the screw geometry: this latter has been evaluated starting from the draft of the EJOT® External TORX Plus® 12EP, peculiarly for an M5x25. Successively, different measures and schematizations were done, to best approximate each sector of the screw in relation either to the designed function (namely

Piercing, Thread Forming and Joint Fastening) or to being a transition surface between two “functionals”: the result is in Figure 10.

To schematize the four lobed tip’ profile, two different parametric curves were adopted, both based on the coordinate x lying on the screw’ axis, while the coordinate y describes the vertical distance from its axis: the former resulted as a degree 4 polynomial,

$$y = p_1x^4 + p_2x^3 + p_3x^2 + p_4x + p_5 \quad (2)$$

which, adopting the coefficients listed in Table 1. and for the data retrieved from the draft, demonstrated high quality in the profile approximation (R-square = 1).

Table 1. Coefficients employed in Eq. 2.

| p_1 | p_2 | p_3 | p_4 | p_5 |
|--------------|---------------|---------------|--------------|-------|
| $1.88e^{-4}$ | $-1.83e^{-3}$ | $-4.14e^{-2}$ | $6.32e^{-1}$ | 0.0 |

On the opposite, the latter was computed as another degree 4 polynomial,

$$y = p_6x^4 + p_7x^3 + p_8x^2 + p_9x + p_{10} \quad (3)$$

and, with the $p_6 \div p_{10}$ values reported in Table 2., demonstrated again an R-square of 1.

Table 2. Coefficients used in Eq. 3.

| p_6 | p_7 | p_8 | p_9 | p_{10} |
|--------------|--------------|---------------|--------------|----------|
| $5.34e^{-5}$ | $1.89e^{-3}$ | $-7.15e^{-2}$ | $6.65e^{-1}$ | 0.0 |

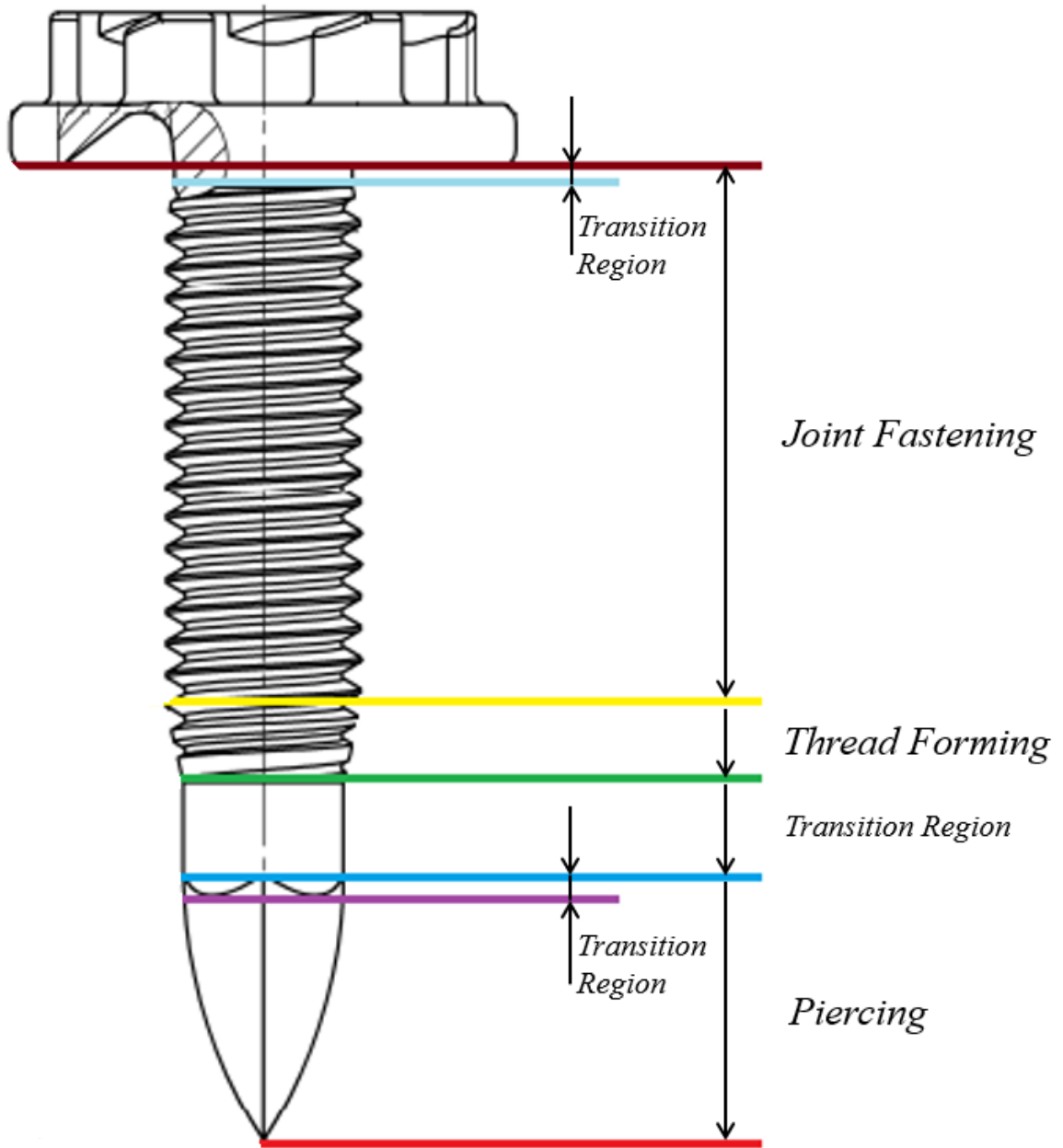


Figure 10. Functional sections of the EJOT TORX Plus 12EP, M5x25

These two profiles are alternated four times per screw tip' rotation, and they can be used to simplify the complete tip geometry; they are engineered respectively to deform the workpieces' material (profile of Eq. 2) and allow it to slide around the screw (profile of Eq. 3), so that to reduce the drilling work by better exploiting the frictional heat generated. In this manner, they are fundamental for the sake of introducing the most important tribological innovation in this field: the *combined Stick-Slip contact condition*. By following this approach, the axial force exerted by the machine on the screw is transposed in shear deformation (leading to plastic deformation of the workpiece) during *sticking*, while in frictional sliding (with no induced plastic deformation) while *slipping*; the transition slipping-into-sticking and vice-versa is induced by the product of Friction Coefficient μ , between screw and workpiece, and Normal Pressure p_N , exerted on the sheet, exceeding the material shear Yield Strength τ_y . This results in shear contact stress τ_{contact} being equal either to $\mu \cdot p_N$ or to τ_y , as exposed in Table 3. The two contact conditions can be traced back to the two different profiles of Eqs. 2 and 3, for which sticking would be related to Eq. 2 and slipping to Eq. 3.

The combined effect of these two contact conditions is inferred from the separate modelling of the FDS technique in full sticking or in full slipping: the former method results in overall torque over-estimation, apart in the starting phase of thread forming process, while the latter induces a general torque under-estimation, excluded the part relative to screw assembling.

Table 3. The combined Stick-Slip contact condition.

| Contact Condition | Interaction Criteria | Contact Shear Stress | Heat Generation Mechanism | Plastic Deformation |
|-------------------|----------------------|----------------------------|---------------------------|---------------------|
| Slipping | $\mu p_n < \tau_y$ | $\tau_{contact} = \mu p_n$ | Frictional sliding | NO |
| Sticking | $\mu p_n > \tau_y$ | $\tau_{contact} = \tau_y$ | Shear deformation | YES |

Neglecting the Screw Tightening phase, whose model will be subsequently exposed, the combined contact condition is necessary to describe the Piercing phase in an appropriate way, mainly due to the screw's Zinc flake coating, which is damaged during the assembling, up to disbanding itself at temperatures above 250 °C: even working with “soft materials” (such as Aluminum 5000 alloys), temperatures higher than 300 °C are encountered [6].

Talking about Hole Drilling phase, the parametric curve from Eq. 2 was chosen to describe the sticking condition accordingly to its pronounced shape, while that from Eq. 3 has been considered more appropriate for the slipping condition. By analyzing a real Torque-Time curve in Piercing, after a first moment of sticking (dictated by the workpiece's temperatures lower than 250 °C), the trend is sinusoidal, with a period

correlated to the rotational speed: as instance, for 8000 rpm, the period S can be demonstrated as

$$S = \frac{1}{f} = \frac{60 \frac{s}{min} \cdot 1000 \frac{ms}{s}}{8000 rpm} = 7.5 \frac{ms}{cycle} \quad (3)$$

so that a sinusoidal, time-dependent function $f(t)$ can be used to simulate this trend, as

$$f(t) = \sin \left(2\pi \cdot \frac{t}{7.5 ms} \right) \quad (4)$$

where t is the time elapsed from the starting, measured in milliseconds. It is additionally assumed that sticking condition corresponds to a torque M increase, while slipping to M overall decrease.

Then, the Friction Coefficient μ for sticking is investigated; typical reported μ for Steel parts on Aluminum parts is around 0.65, while the Friction Coefficient between Zinc-coated Steel and Aluminum is approximately 0.15: the model is designed to evaluate, as temperature and time dependent, the most appropriate Friction Coefficient as related to the hypothetical wear of the Zinc coating. The resulting curve is similar to the common Tool Wear characteristic curve, and as that, it can be subdivided into three regions, from initial rapid wear (*Break-in Period*) to uniform wear rate (*Steady-state Wear Region*), until final accelerated wear rate (*Failure Region*). For this case study, the curve was transposed from [6] up to $\mu = 0.5$ for $T=250$ °C as “Coulomb Friction Model”, then a “Shear Friction Model” was chosen, for which $\mu = \text{constant}$ for those $T > 250$ °C.

After the transition region from the screw' tip, constituted by a conical surface shaping the tip' four-lobed section into a circular section, plus the cylindrical part itself, overcomes the upper sheet' upper surface, Thread Forming in the just drilled hole starts: it is characterized by a decrease of the rotational speed (within a stated Ramp Time) to a middle value (around 2000 rpm), and it is performed by the section of the screw including not-complete threads, necessary to correctly guide it into the hole and gradually deform the surrounding material; in the CAD, these latter have been recreated firstly as a conical smooth surface, then as three subsequent threads with increasing nominal diameter, up to the standard M5 one.

When the threads are completely formed, the torque decreases thanks to the low Zinc-Steel Friction Coefficient, and after a constant path in which the extrusion is modeled under the screw' head, Tightening starts: it adopts a simple Torque Control method, in which the machine stops when its loadcell detects the desired torque value (and thus Preload) has been reached; the formulation is similar to the usual one, but influenced by the peculiar contact happening under the head (Eq. 5).

$$M_{tot} = M_{pitch} + M_{thread} + M_{head} = F \left(\frac{p}{2\pi} + \frac{\mu_t r_t}{\cos\alpha} + \mu_b r_b \right) \quad (5)$$

where the total torque M_{tot} has contributions depending on the pitch, the thread' shape (with r_t as the effective thread radius, half of d_t and in [mm]) and the area of contact with the screw' head (with r_b as the underhead mean contact radius, in [mm], and μ_b as the corresponding friction coefficient).

1.3 Objectives

After having introduced and explained the complex FDS technique, the objective of this research is to develop a working and valid FEA Model within the innovative MSC Simufact Forming software, version 2020, for the piercing phase: this introduction within an industrial environment, namely in Process Development phase, would cut time and costs that otherwise should be spent to perform an experimental testing campaign.

As a starting point, the author will introduce the necessary experiments required as evidence and reference for simulation comparison. These tests include measurements on temperatures, performed with thermocouples. Then the research proceeds with the lower sheet AW6082-T6 description in terms of its mechanical properties, which include its True Stress-Strain curves and its temperature-dependent Young Modulus.

Further, a CAD geometry of the screw is derived with the considerations exposed in Section 1.2, and the Friction law governing its contact with the lower sheet is included in the FEA model. Next, the step-by-step setting of the model is presented, together with criteria for acceptability of the simulation results (including assembling axial force and shape factors) and the basis for a Fractional Factorial analysis to evaluate and study the effect of relevant simulation factors on the real piercing phase. Finally, the developed model is used to study the effect of its characteristics, as for instance Friction laws and workpiece thickness, on the process results. The target is to obtain a validation of the hypotheses done, particularly the combined Stick-Slip contact conditions between screw and lower sheet. Also, the limitations that come from the use of a 2D axisymmetry FEA model to study the process are discussed.

CHAPTER TWO

METHODOLOGY

2.1 Experimental set-up

For what concerns the model validation, two experiments were performed in CRF Laboratories in Melfi (Italy): the main properties of the materials employed are reported in Table 4., while the complete experimental apparatus, as well as the specimen's dimensions and geometry, are indicated in Figure 11. For each testing condition, three repetitions were done to give statistical confirm of the results.

Table 4. Main properties of the materials employed.

| Name | Description | Thickness, [mm] | Yield strength, [MPa] | Ultimate Strength, [MPa] | Density, [kg/m ³] |
|-----------|---|--------------------|--------------------------|-----------------------------|----------------------------------|
| DP600 | Cold rolled Steel, Dual Phase; pre- drilled hole | 1.5 | 330 up to 440 | 590 up to 700 | 7600 |
| AW6082-T6 | Extruded Al alloy; T6 = heat treated, quenched and artific. aged | 2.0, 3.0 | 200 up to 250 | 300 up to 350 | 2700 |

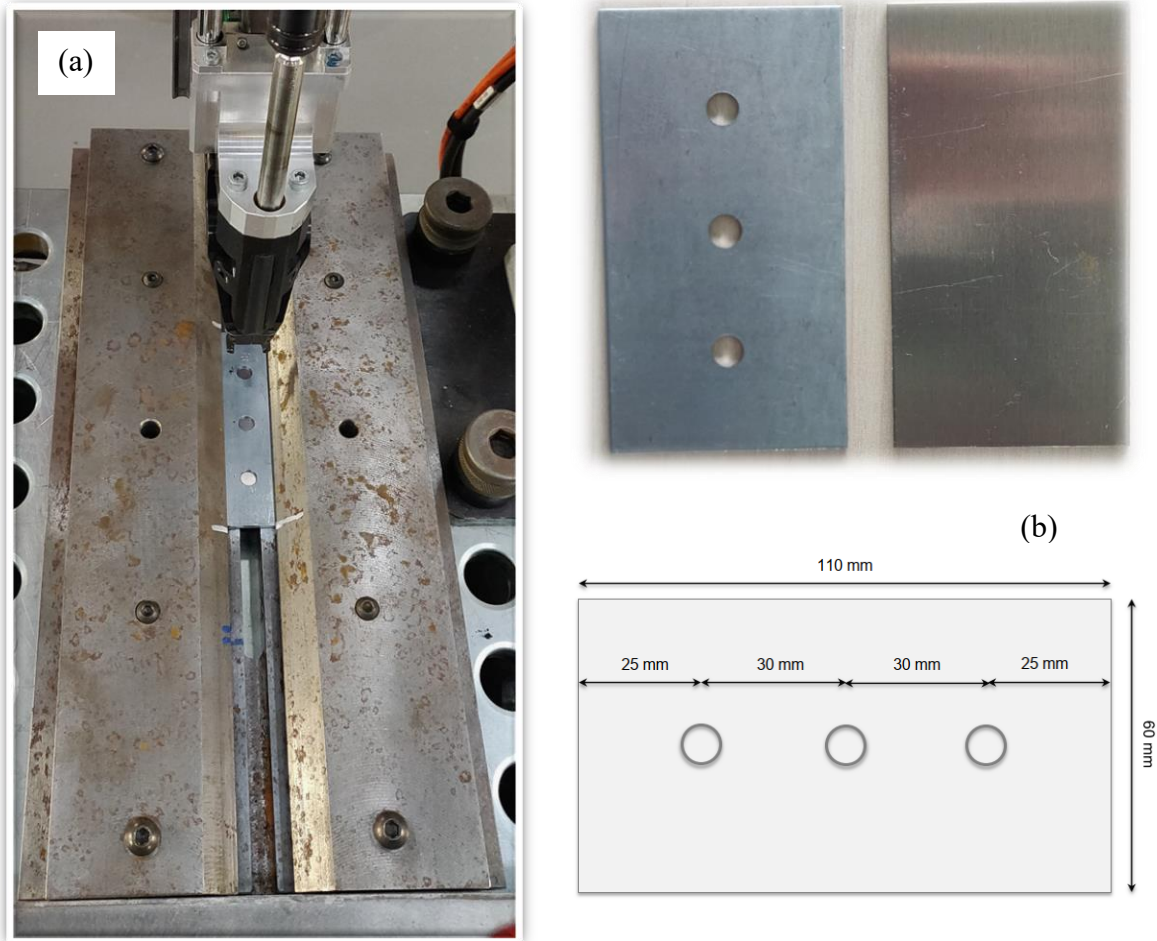


Figure 11. The experimental apparatus (a) and specimen (b).

The first experiment was pointed at studying the screw' piercing in a 2.0 mm thick AW6082-T6 plate, so that the RSF21 machine was programmed to stop at around 11.5 mm of penetration, as it comes by considering the 1.5 mm thick DP600 plate plus 10 mm long screw's tip. Different input parameters were chosen, varying rotational speed and

applied axial force: they are reported in Table 5. The picture of an example of successful hole drilling is shown in Figure 12.

Looking at the results reported in Table 5, it is to be noted that P43 setting parameters were not high enough to achieve complete piercing (see the picture of Figure 13), while all the other configurations resulted as successful.

Table 5. The experimental tests' input parameters.

| Test Code | Rotational Speed, [rpm] | End Load, [N] |
|-----------|-------------------------|---------------|
| P41 | 6000 | 750 |
| P42 | 8000 | 600 |
| P43 | 5000 | 600 |
| P44 | 8000 | 750 |

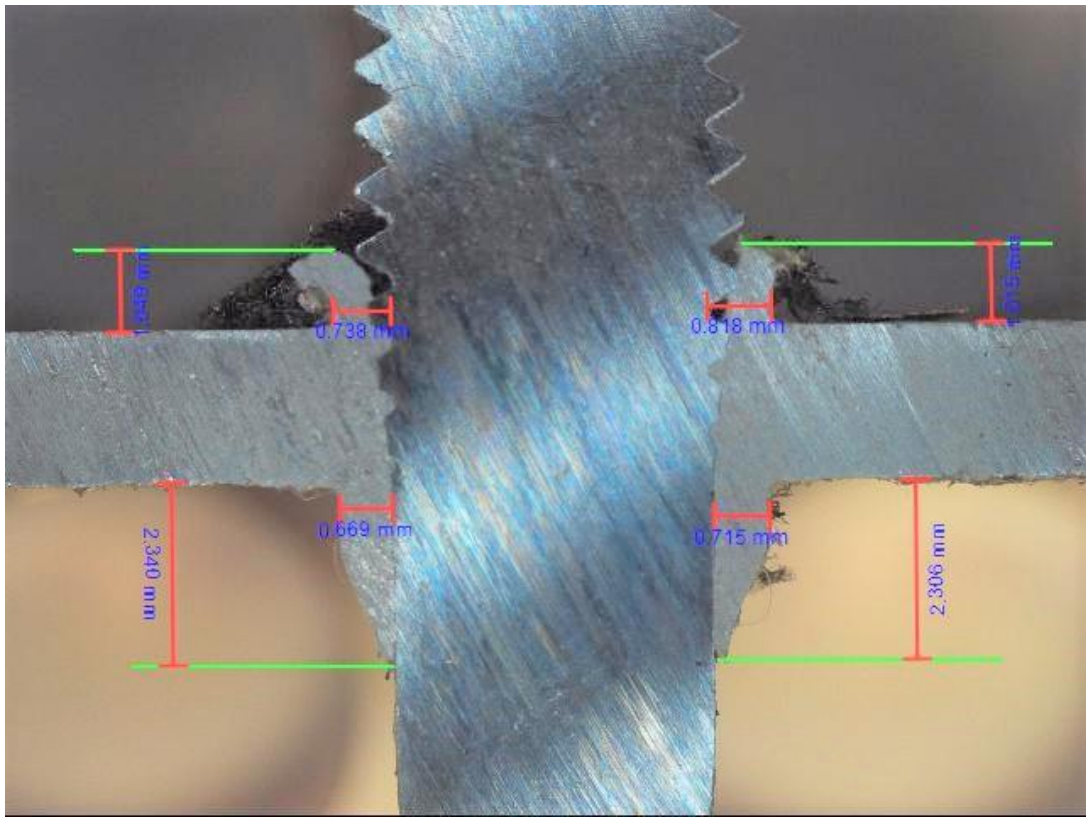


Figure 12. Macrograph of P44 - successful piercing test.

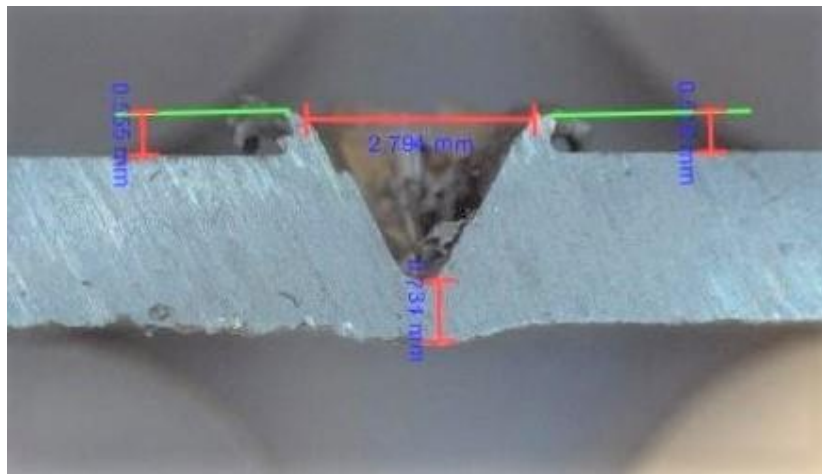


Figure 13. Macrograph of P43 - unsuccessful piercing test.

The second experiment was focused on the complete Flow Drill Screwdriving[®], with correlation among depth, rotational speed, axial force and applied torque. This was necessary to analyze the temperature variation due to the frictional heat: thermocouples were positioned at approximately 10 mm from the joint center on the lower sheet' lower surface, so that to measure the peak as well as the period of temperature rise and fall. The parameters set-up is the same of Case P44, the difference lays in the lower sheet's thickness of 2.0 mm (Case P34) and 3.0 mm (Case P35). The experimental apparatus is visible in Figure 14a, Figure 14b shows a macrography of the completed assembling. In Figure 15 the characteristic trend of the temperature curve is presented. A quick rise of the temperature (about 60 °C in 2 s) can be observed, followed by a smooth decrement.

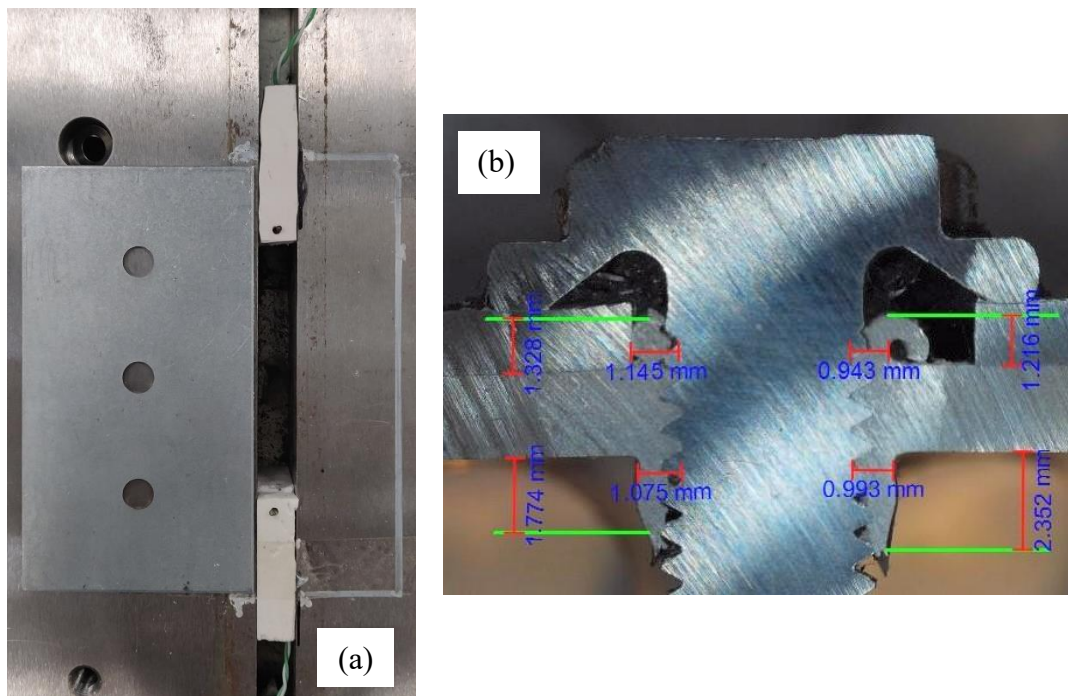


Figure 14. Thermocouples position (a) and macrography (b).

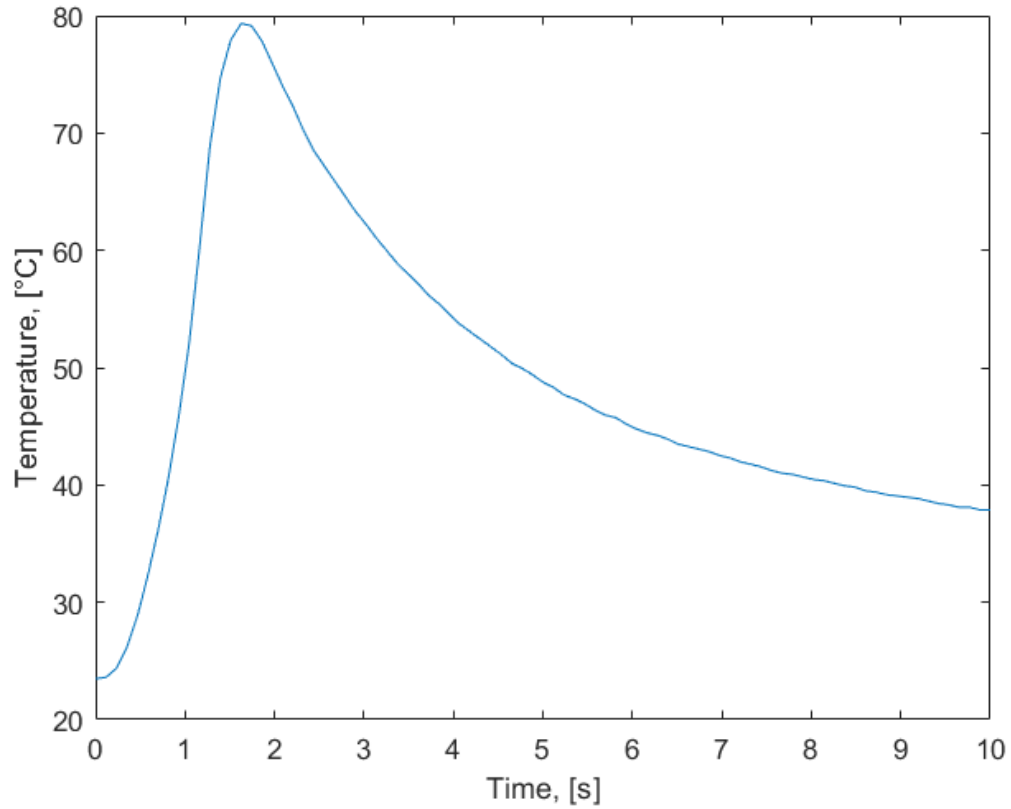


Figure 15. The Temperature-Time curve of test P34, at radial distance of 10 mm.

Now it is necessary to focus on the lower sheet' material : the AW6082-T6. It has to be defined in terms of all its mechanical properties, whose majority is retrieved from [14] and already present inside Simufact database. As CRF laboratory provided the Engineering Stress-Strain Curve, the True Stress-Strain Curve comes with Eqs. 6 and 7.

$$\varepsilon = \ln(1 + e) \quad (6)$$

$$\sigma = S(1 + e) \quad (7)$$

In this case, the material is defined for strain rate $\dot{\epsilon} = 1.0 \text{ s}^{-1}$ and $T = T_{room} = 20 \text{ }^\circ\text{C}$, but during the whole process, different conditions are to be encountered: the *Johnson-Cook Model* (abbreviated J-C Model) is thus adopted to formulate the True Stress-Strain relation for every temperature and strain rate, but only within the curve' Plasticity Zone. The complete formulation of the J-C Model is in Eqs. 8 and 9, assuming $\dot{\epsilon}_0 = 1.0 \text{ s}^{-1}$

$$\sigma_{pl} = (A + B\varepsilon_{pl}^n) \left[1 + C \ln \left(\frac{\dot{\epsilon}}{\dot{\epsilon}_0} \right) \right] (1 - T^{*m}) \quad (8)$$

$$T^* = \frac{T - T_{room}}{T_{melt} - T_{room}} \quad (9)$$

with A, B, C, n and m as material-dependent parameters to be experimentally evaluated and temperature-independent, while T_{room} and T_{melt} are respectively room and material melting temperatures.

Since needed within the combined Stick-Slip contact condition, the shear stress in the Plasticity Zone τ_{pl} is computed coherently with Von Mises formula, i.e., with Eq. 10.

$$\tau_{pl} = \frac{\sigma_{pl}}{\sqrt{3}} \quad (10)$$

The material-dependent parameters of Eq. 8 have been derived from [15], with the adaptations presented in Table 6. to comply with CRF experimental curve and considering the material as strain-rate independent (that is, with $C = 0$).

Table 6. J-C Model Parameters for AW6082-T6.

| A , [MPa] | B , [MPa] | n | m | T_{melt} , [°C] |
|-------------|-------------|-------------|-----|-------------------|
| 290.72 | 304.9 | $6.8e^{-1}$ | 1.3 | 650 |

Regarding the Elasticity Zone of the $\sigma - \varepsilon$ curve, the Young' Modulus dependency on the temperature was evaluated starting from the data found in [16] with a fitting polynomial equation of degree 4, whose coefficients are in Table 7 and the resulting curve is in Figure 16. The curve fitting was made possible thanks to the homonymous MatLab[®] Tool, which reported an Adjusted R-square of 1.

Table 7. Coefficients for Young Modulus - temperature fitting polynomial for AW6082-T6.

| p_1 | p_2 | p_3 | p_4 | p_5 |
|---------------|--------------|---------------|-------|----------|
| $-1.09e^{-6}$ | $1.71e^{-3}$ | $-8.44e^{-1}$ | 8.84 | $7.6e^4$ |

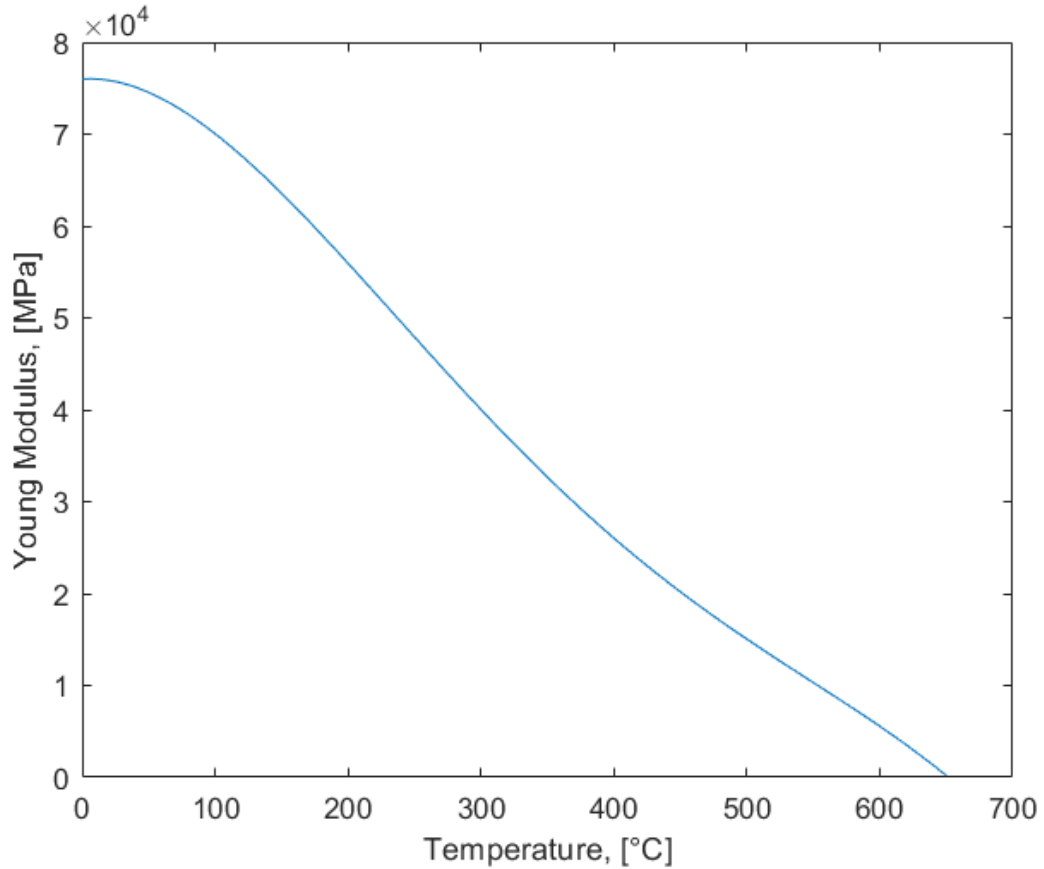


Figure 16. Young Modulus of AW6082-T6 *versus* temperature.

The complete True Stress-Strain curves, for different material temperatures, are finally obtained by combining the Elasticity and Plasticity Zone' curves at each temperature: from the linear σ - ε relation of the Elasticity Zone that is drawn taking into account the Young modulus' value as function of the temperature, then the Plasticity Zone transition is defined from when the calculated σ_{pl} for a given ε is minor or equals the calculated $\sigma_{el} = E \cdot \varepsilon$, once again remembering the modification induced by the temperature. The results are presented in Figure 17, where the T=20 °C curve refers to the experimentally evaluated values.

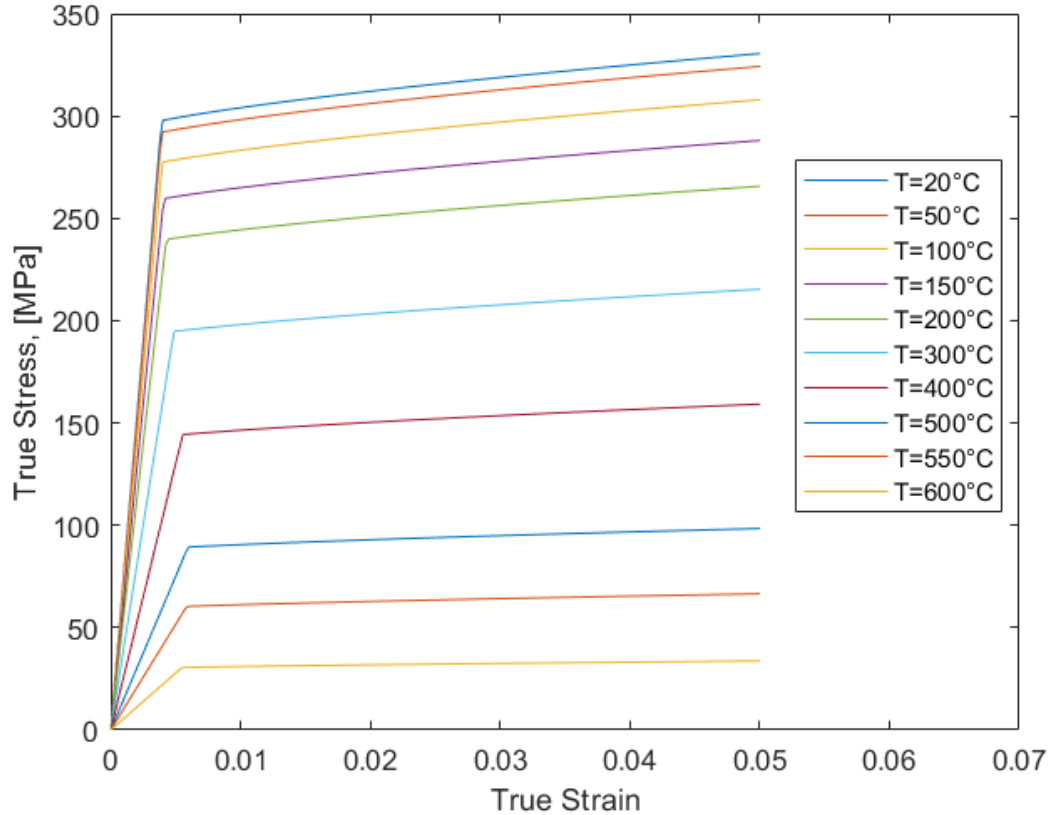


Figure 17. $\sigma - \varepsilon$ curves at different temperatures for AW6082-T6.

2.2 CAD and Numerical Model development

In the material forming software adopted for this research, the FEA simulations start from modules reproducing common industrial processes, in which all the useful data are inserted in a *process tree*. In the present case, the best module to be used is *Friction Welding*, which obeys to the Pressure Welding rules: two different *workpieces* have to be defined, namely the FDS and the lower sheet; the former is intended to heat up thanks to friction at rotational sliding on the latter, and finally its surface material to melt and create a stable bond (feature disabled in this work). Next, the *die insert* is chosen as the socket, whose CAD had previously been developed by surface subtraction of the screw's

head on a cylinder: its real function is to apply axial force, rotational speed and torque from the assembling machine on the screw but, as the process is here formulated as Time-Depth dependent, its role can be compared to a dynamometer'. Its inner border presents a fillet at screw contact to avoid high punctual stress; this element is assigned to a user-defined *press* function, through which the time-stroke relation is set (Fig. 18). Finally, both platen (in the FEA model, reported as *Table*) and blank holder are added to the assembly as rigid elements with heat transfer.

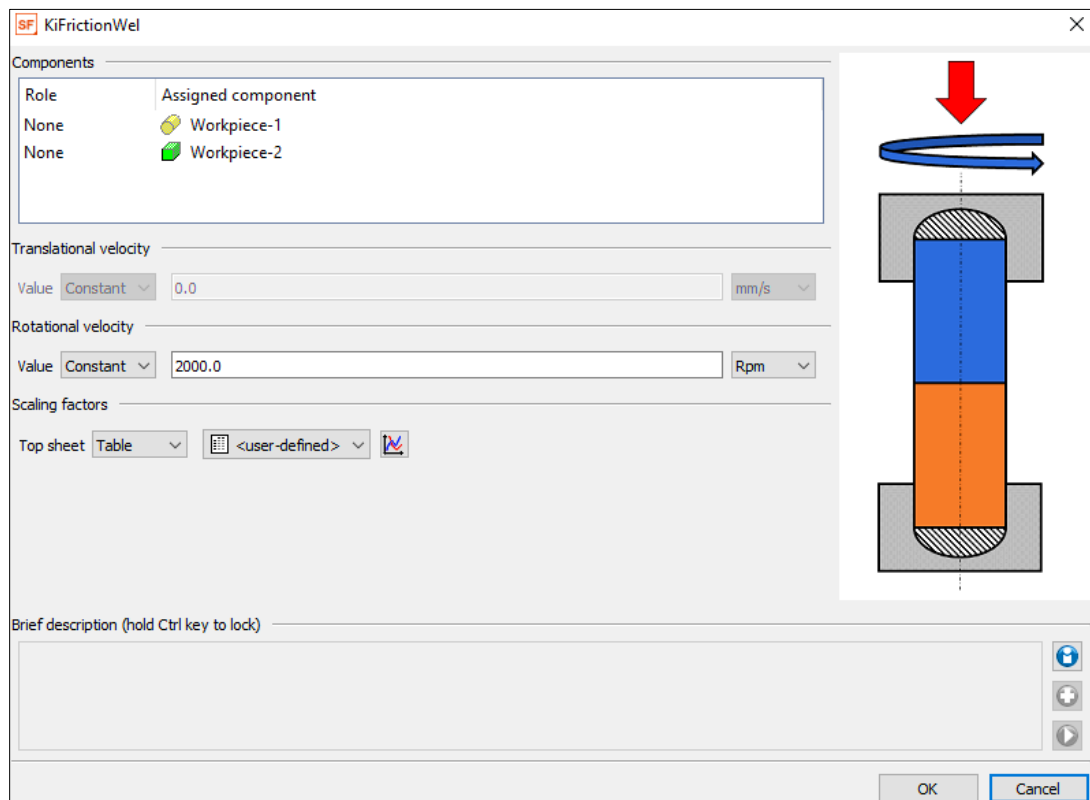


Figure 18. Friction Welding module' main settings.

As key point of this work, the combined Stick Slip contact condition has to be implemented in the calculations, peculiarly in the evaluation of contact behaviors between screw and workpiece: as from the data available in [6], the Coulomb friction coefficient μ has been expressed as temperature dependent, with a relation as shown in Figure 19 and valid until 250°C. After this point, due to increasing plasticity of AW6082-T6, a friction model centered on shear can be more effective, so that the option of *Combined Coulomb-Shear* contact relation has been selected: the contact is governed by Coulomb Law until a given shear value is reached, after which the contact condition becomes $\tau = m \cdot \frac{\sigma_U}{\sqrt{3}}$, with m as Interface shear factor, ranging between 0 and 1, and σ_U as workpiece material' Ultimate shear strength.

The Interface shear factor was initially chosen as 0.2 to respect the software database suggested value when considering Steel-to-Aluminum contact conditions, since the FDS Zinc coating disbands for $T > 250^\circ\text{C}$ (as previously stated and evidenced in [6]).

The screw' tip has been considered axisymmetric thanks to the lobes' symmetry, so that computations can be sped up by simulating the Piecing process in 2D FEA with a section of the CAD assembly. The symmetry plane has been chosen to contain one of the four sticking profiles of the tip (expressed in Eq. 2), so that to achieve a gradual hole drilling; by choosing any other profile curve of the screw' tip, the conical surface of transition to the smooth cylindrical section could result in mesh-related issues (as elements' extreme distortion) and finally lead to computations' lack of convergency.

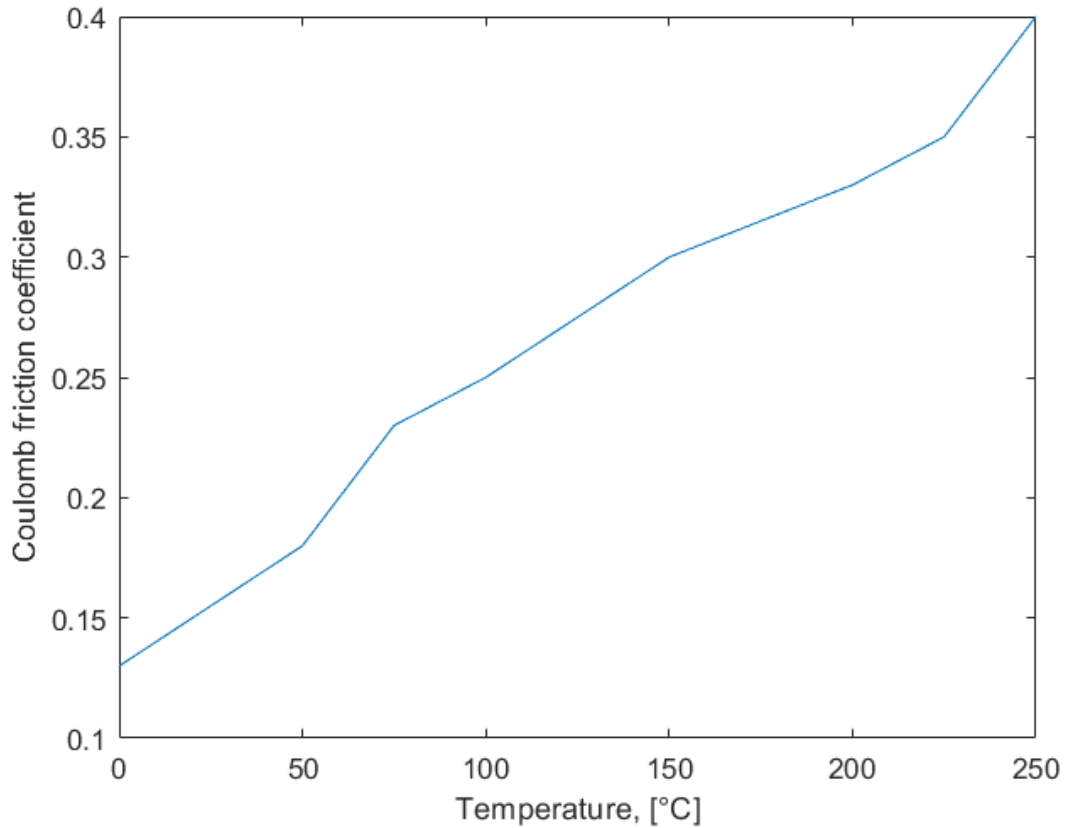


Figure 19. Adopted Coulomb' μ - temperature relation.

The whole CAD assembly is presented in Figure 20, with the specimen formed by DP600, 1.5 mm thick pre-drilled upper sheet and AW6082-T6, 2.0 mm thick lower sheet.

The drawback that comes from the adoption of 2D axisymmetric option is the neglect of some factors: apart from the two main tip' profiles alternation, the transversal deformation and displacement of the workpiece' material is not evaluated, and so the consequent energy dissipation is not considered. The highest influence of this simplifying hypothesis has been encountered on the axial force (the End Load) exerted by the socket on the screw in the piercing phase, which does not present the usual oscillatory behavior.

As consequence of this drawback and taking into account the typical spread of experimental outputs for even similar testing conditions, a 30% threshold for the peak registered value has to be introduced when comparing the FEA versus experimental data, while a maximum threshold of 2 kN has been established. The complete list of imposed evaluation criteria for the FEA simulation' results is given in Table 8.

The frictional heat in Simufact Forming is not calculated by the tool movement, but by using a specific formula, which, when adopting the peculiar Friction Welding module, is governed by the tool' *rpm* and the *Scaling Factor* (SF). This latter, as temperature-dependent parameter combining the friction coefficient used for the heat calculation, the efficiency and user defined factors, ranges from 0 to 1. It is useful to partially recover from the lack of those factors implied by the 2D axisymmetry hypothesis. The SF is augmented to increase the calculated temperature in a node, thus it must go to 0 when $T > T_{melt}$, since no frictional heat generation is considered in the material at this state.

At first, a heatmap study has been conducted for SF values in the range (0.1 ÷ 0.4), observing the effect of this sole parameter on the numerical simulations: the aim is to determine the lowest admissible SF (to minimize user-dependent factors) while pursuing the accuracy to experimental specimen geometry, along with Target and Monitoring parameters' measures. In the heatmap, "Pass" was attributed to cases in which all the conditions exposed in Table 8 were achieved, "Part. Fail" for those having just the max End Load higher than 2 kN (an issue commonly met in these FEA simulations, but not negligible), while "Fail" for all the others.

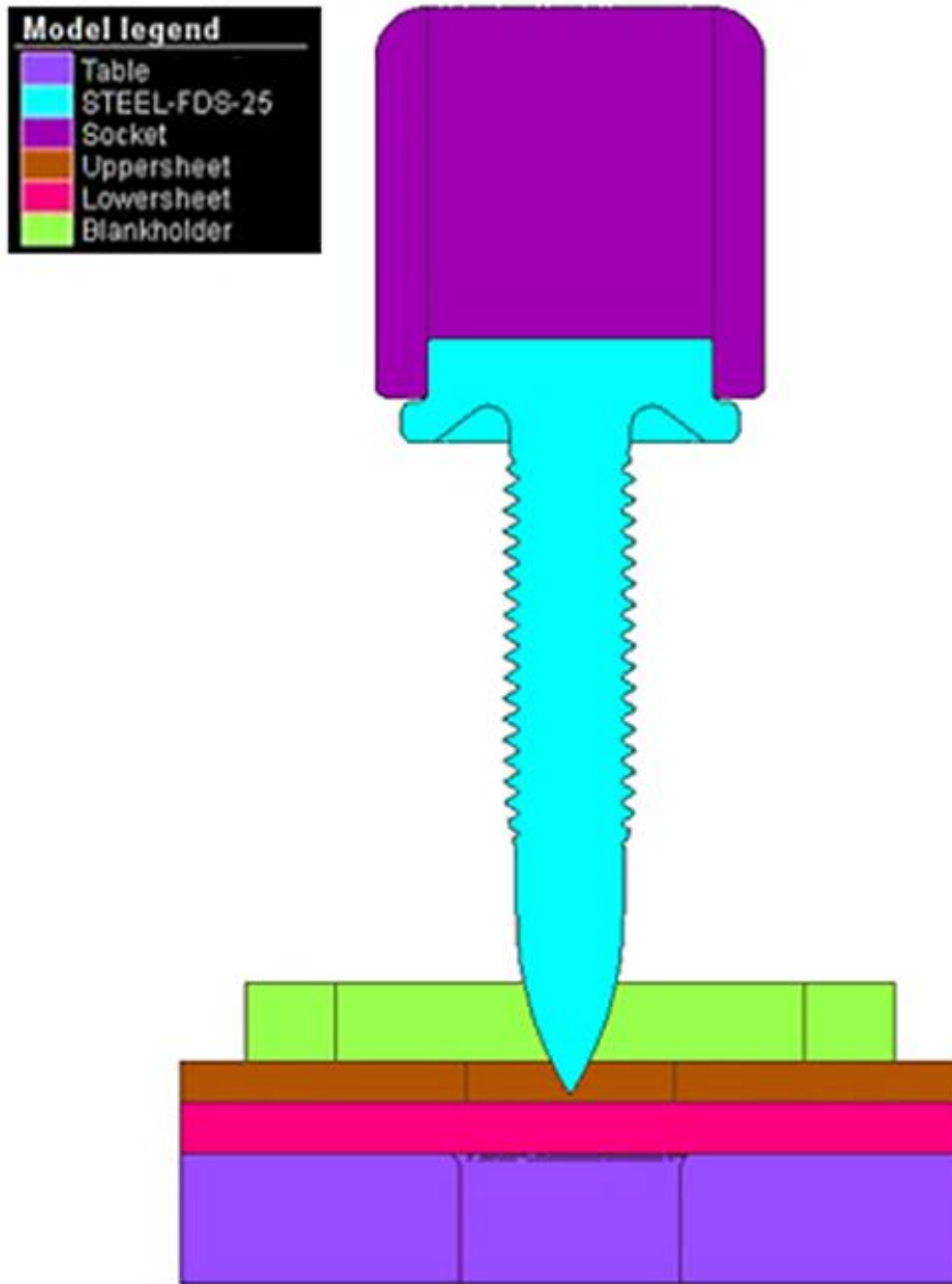


Figure 20. Section of the modeled assembly.

Table 8. FEA Simulations' required acceptance criteria.

| Nature | Criteria | Description |
|--------------|---|---|
| Mathematical | Calculation Convergency | Simulation must reach 100% completion rate |
| Geometrical | Extrusions shape | Best accuracy with experimental evidence (dimensions and shape) |
| Geometrical | No material removal | Avoid material detaching from the extrusions |
| Physical | Max workpiece temperature | Shall not exceed 400°C (adapted from [6]) |
| Physical | Max workpiece temperature at Thermocouples position | Shall be within the experimental value $\pm 10\%$ (seen in Figure 15) |
| Physical | Peak End Load value | Shall not exceed 2 kN |

Afterward, the effects of different process and numerical simulation' parameters both on FEA and real Piercing results have been determined via a Factorial method, including 5 different factors (as seen in Table 9.) assuming a "Low" and a "High" value; for each combination, a single repetition was conducted, as the FEA model had already been studied and proved robust. While choosing a Full Factorial analysis would require 2^5 tests, and, thus, 32 different simulations, a $\frac{1}{4}$ Factorial was employed, requesting only 2^3 runs but implying that the statistical dependency of simultaneous factors' interactions with the output cannot be analyzed. The "Low" values for Coulomb friction coefficient and Interface friction factor were assumed from [17].

Table 9. Factorial analysis' factors

| Factor ID | Name | Abbreviation | “Low” value | “High” value |
|-----------|------------------------------|--------------|-------------|--------------|
| A | Scaling Factor at 0 °C | SF_0 | 0.1 | 0.2 |
| B | Scaling Factor at Melting | SF_Melt | 0.1 | 0.2 |
| C | Coulomb friction coefficient | mu | 0.1 | 0.4 |
| D | Interface friction factor | m | 0.2 | 0.4 |
| E | Screw rotational speed | rpm | 6000 | 8000 |

Now, the requested outputs had to be both at least as possible to obtain the most trustworthy and straight-forward factorial analysis results, but also enough to fully achieve the “success” in FEA simulations; thus, the following were chosen:

- “Success Percentage”, indicated as *Perc*; its possible values are 1 for FEA successful run, 0.9 when only max End Load is exceeded, 0.75 for all the other cases in which calculations convergency is still verified, and 0.5 otherwise.
- Workpiece’ upper extrusion height, expressed in [mm] and with the term *L1*; measured from the upper flat surface to the upmost extremity (Figure 21).
- Workpiece’ lower extrusion height, expressed in [mm] and with the term *L2*; measured from the lower flat surface to the lowest extremity (Figure 21).

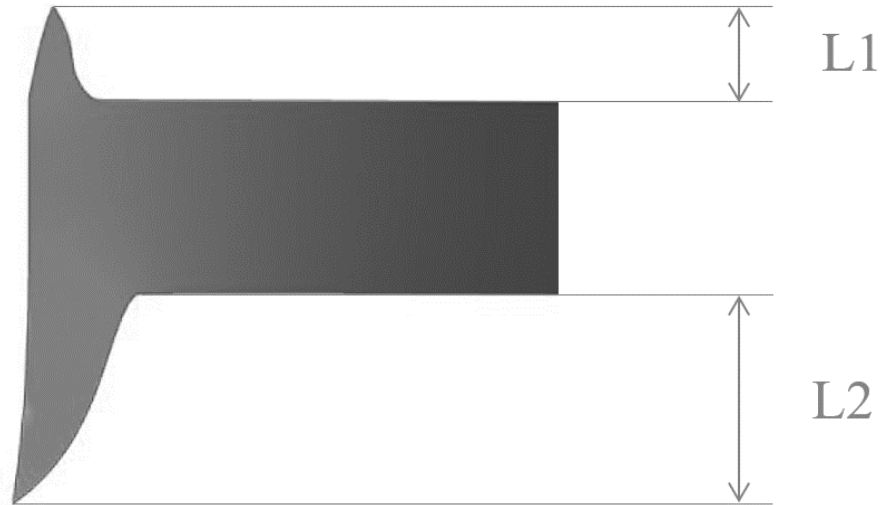


Figure 21. L1 and L2 geometrical meaning.

The Factorial analysis was run within Minitab[®] environment, considering the software-indicated center point as well ($A=0.15$, $B=0.15$, $C=0.25$, $D=0.3$, $E=7000$); thanks to the options available in the software, a Factorial optimization was additionally done, with target outputs values as 1 for *Perc*, and 0.95 mm and 2.3 mm respectively for *L1* and *L2*, as averages of experimental evidence values (in detail, from P41, P42 and P44).

To conclude the 2D Axisymmetric study, last FEA simulations were run aiming to:

- Determine whereas a simulation run with rigid screw, having *heat conduction* feature on, can perform better in terms of Computational Time and respect of acceptance criteria than another with deformable screw.
- Study the effect of whether the AW6082-T6 is modelled with or without the introduction of a Damage Criterion for material detachment; peculiarly, the normalized Cockcroft-Latham Fracture criterion was chosen (Eq. 11) among the

different options available in the software; in that equation, σ_1 , in [MPa], is the maximum principal tensile stress, $\bar{\sigma}$, also in [MPa], is the effective stress, $\bar{\epsilon}_{fract}$ is the equivalent strain at fracture and $\bar{\epsilon}$ is the equivalent strain; the value for nCL is taken from [18].

$$nCL = \int_0^{\bar{\epsilon}_{fract}} \frac{\sigma_1}{\bar{\sigma}} d\bar{\epsilon} \quad (11)$$

- Validation of the relation Coulomb friction coefficient - temperature as taken from [6], with comparisons both with non-temperature dependent friction coefficients and with the same material (AW6061-T6) used in that research.
- Evaluation of the effect of 3.0 mm thick lower sheet with respect to 2.0 mm thick, as well as with wider workpiece.
- Evaluation of the effect of different rotational speeds, namely 5000 rpm (from [6]), 6000 rpm (as previously used within industrial environments) and “nowadays” 8000 rpm.

CHAPTER THREE
RESULTS AND DISCUSSION

According to what said in Chapter 2.2, at first a heatmap for the determination of the Scaling Factor is presented (Figure 22), correlated with the examination of the main defects found in FEA modeling results (Figs. 23 and 24). After a comparison between best simulation result and experimental case (Figs. 25÷29), the $\frac{1}{4}$ Fractional Factorial analysis is exposed and commented (Figs. 30÷33). Finally, the final testing on conditions involving different workpiece material, thickness, etc. are seen (Figs. 34÷47).

The graphs were all computed by using MatLab software when possible, while in some cases Excel[®] has proved necessary to organize the data in a more user-friendly manner. Regarding the images of the model and its outcomes, the tool “Snapshot” of Simufact Forming 2020 was employed for the best quality available, and assembly sections (as product of a 2D FEA simulation) were preferred to partial 3D obtained by extension around Z axis, since being easier to understand, as well as not leading to wrong images: for instance, expanding the 2D screw section would lead to absence of spiral threads and head characteristic shape.

Unluckily, Simufact at last was unable to directly measure the Time vs. Torque graph; moreover, the correlation in the piercing phase is quite complex, as it depends on many features neither easy nor even available for user definition. For these reasons, the author instead reported the Time vs. End Load graph when needing for comparison with the experimental evidence.

3.1 Main factors influencing the simulations

As required to start the work in the material forming software, the Scaling Factor had to be chosen: apart from considering two different points, one at 0°C and the other at AW6082-T6 melting point (650°C), the primitive values were at first refined by trial and error, finally leading to a heat map as exposed in Figure 22. When their importance in correctly reproducing the workpiece material' deformation and displacement induced by the screw tip became clear, a Factorial analysis including three other critical factors was conducted to establish their effect on peculiar outputs.

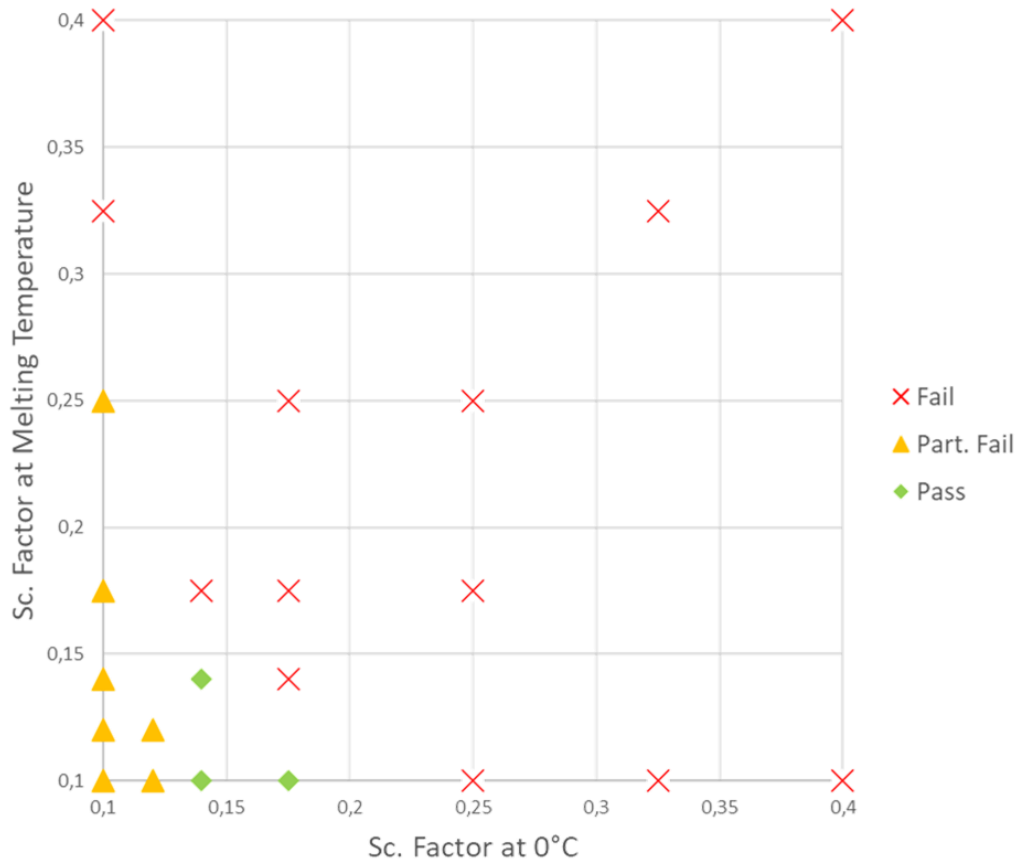


Figure 22. Heatmap for Scaling Factors at 0 °C and Melting Point.

For the graph in Figure 22, the author preferred not to organize the data found into the zones commonly met in heatmaps, as the SF combinations at their boundaries could lead to unpredictable FEA simulation outputs; rather, by organizing the results for single points, the repeatability of each run is ensured.

Now focusing on what has been discovered, the model demonstrated the same width of range of “acceptance” of SF at Melting Point, compared to the one at 0°C, even though all the combinations $SF_{Melt} = (0.1 \div 0.25)$ for $SF_0 = 0.1$ implied over-threshold End Load. It could be noted that for values generally higher than 0.25, the run encounters geometrical and physical failures, which are principally lower extrusion detachment: this can be traced back to workpiece material’ adhesion to the screw, enhanced by the high temperatures reached in those regions, and so linked to too important heat generation by friction (as forementioned in Chapter 2.2). Common failures met in the workpiece are

- Material adhesion (Figures 23a and 23b), which is strictly related to Scaling Factors, and so can be avoided only by carefully tuning them; peculiar case is chip formation (as in Figure 23b), that is, when a small part of lower extrusion material is removed by the screw tip.
- Material self-intrusion (Figures 24a and 24b); while found formerly in the upper extrusion, it is mainly caused by tribological complications at the screw/workpiece contact surface, it is avoided with self-contact definition within the *Contact Table* section.

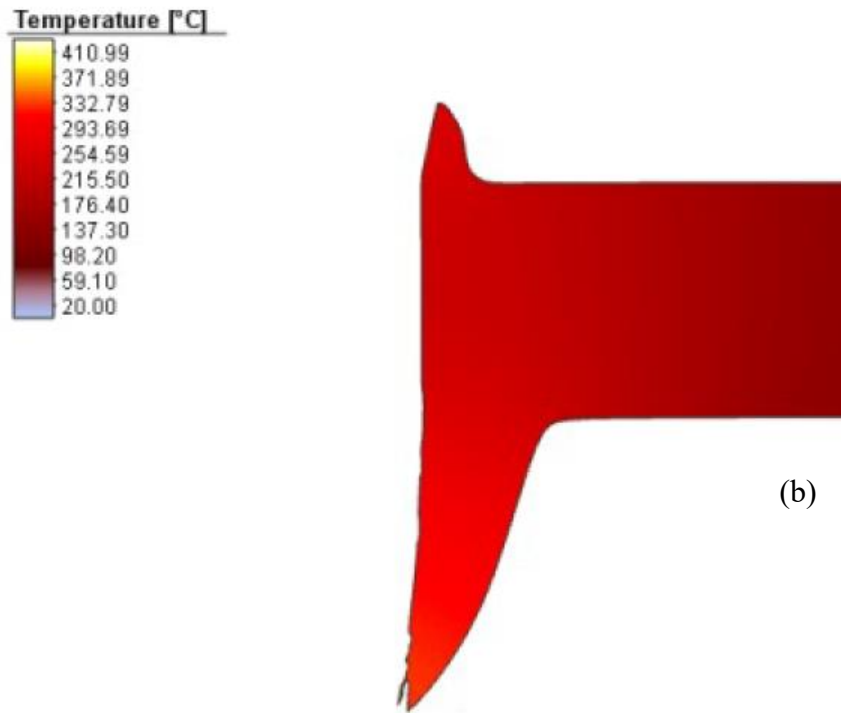
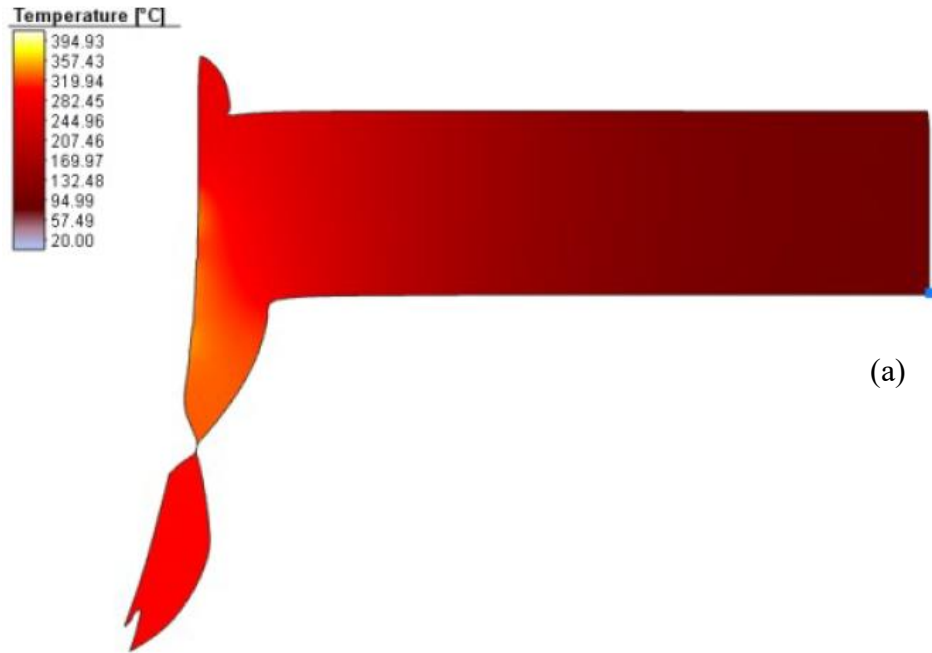


Figure 23. Lower extrusion detachment (a) and chip formation (b).

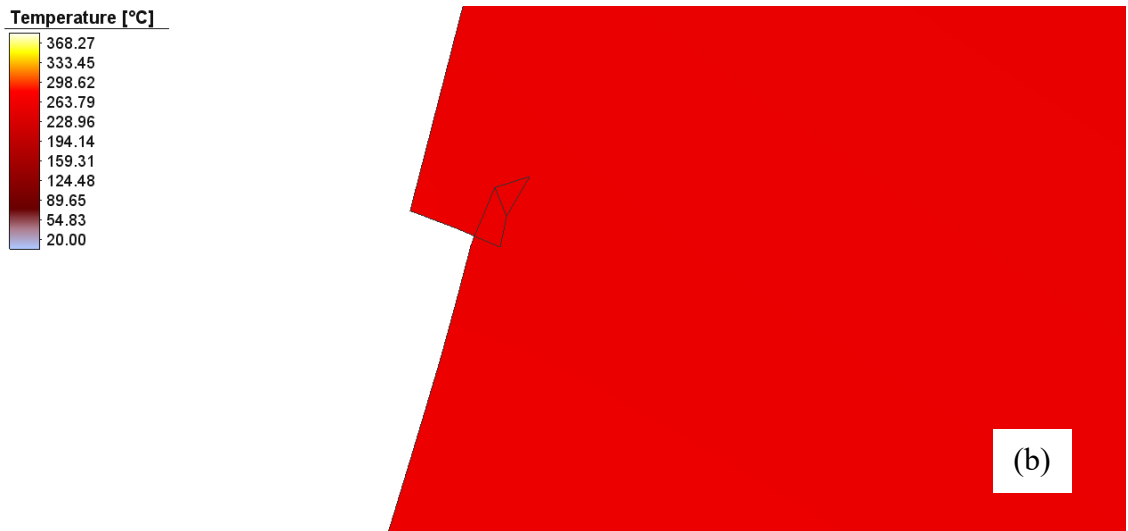
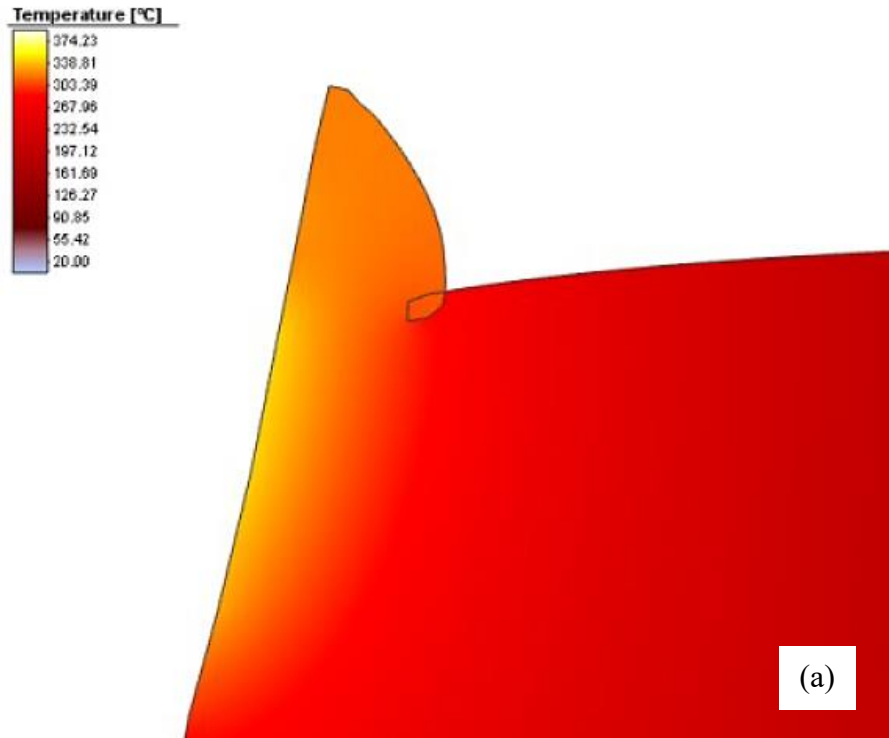


Figure 24. Self-intrusion at upper extrusion (a) and at contact surface with screw (b).

It is now time to analyze a “successful” numerical simulation, that is a run which fulfills the acceptability criteria exposed in the previous Chapter: Figure 25 presents the geometrical aspect, Figure 26 is pointed to the comparison between axial force exerted by the socket versus the log data of RSF21 machine’ dynamometer; last but not least, the temperature trends at the Thermocouples measuring point are compared in Figure 27.

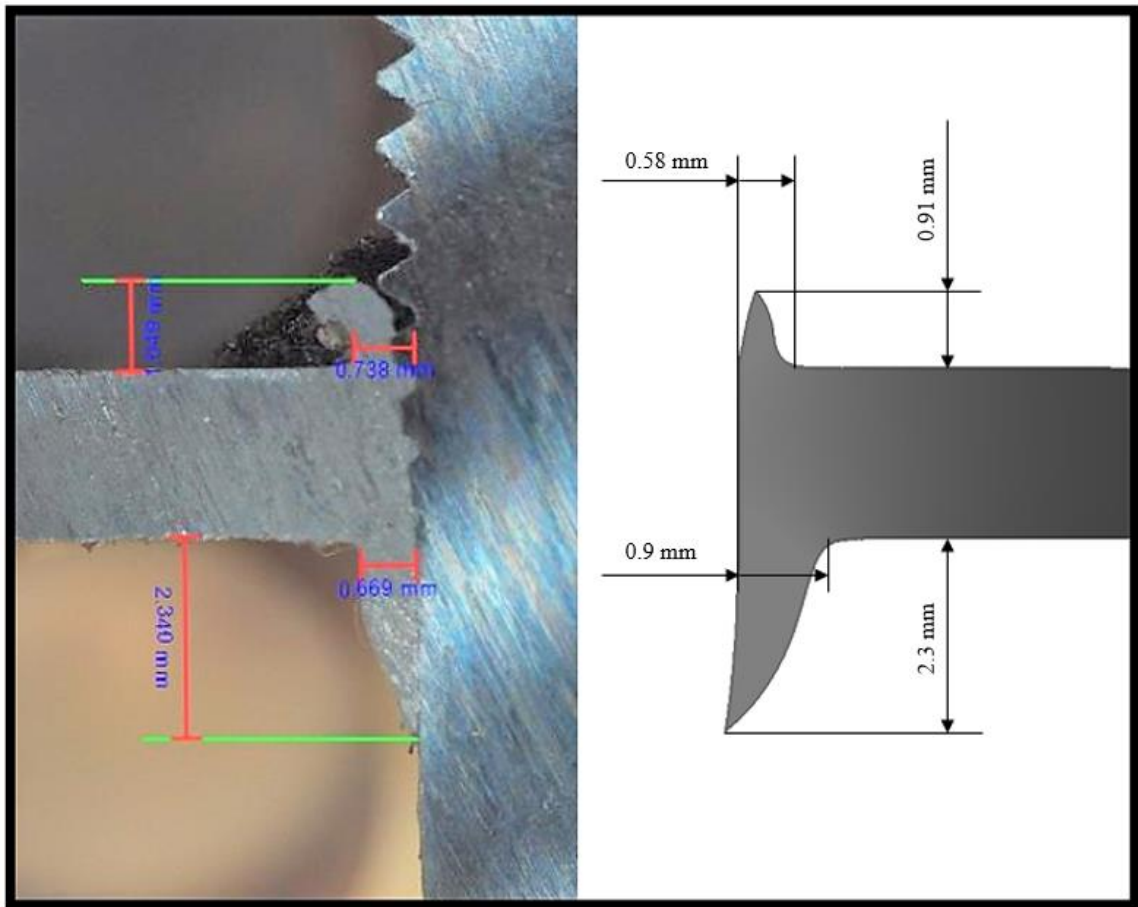


Figure 25. Experimental vs FEA extrusions, geometrical comparison.

The first difference visible between the experimental and numerical simulation geometries is the presence of partial thread forming in the experimental image: this can be explained by the difficulties at setting the assembling machine to definitely stop at completed piercing. This has consequences in the material distribution around the screw, as some more is displaced in the upper extrusion (which is consequently partially bent), while the lower one is straightened by the FDS tip' cylindrical section. In terms of extrusions' height, the two findings are well correlated, so that parameter can be used to verify geometrical correctness of the runs. Regarding the software output, the screw was removed for clearness, while in the experimental test that solution was not possible, as implying extrusions' deformations. In Figure 26, the Z Force oscillations registered in the experiment are reduced to minimum in the simulation: as said before, this is due to the 2D axisymmetric hypothesis, and it is reflected also in the peak value being well higher than in the test. Additionally, the axial force in real experiments is seen oscillating close to its mean during a defined period, then increasing to its maximum: it is due to the pre-assembling procedures before the screw contacts the lower sheet, required to minimize secondary issues, as well as to create an "invite" so that the tip can penetrate with lower efforts; after this step, the peculiar contact conditions, combined with large quantity of material being displaced into the extrusions, lead to End Load increase until reaching a "steady-state" working condition (in the graph, from 400 ms up to the end of the phase), while in simulations the overall FDS work is greatly reduced after the tip' extremity exits from the workpiece (at around the same instant 400 ms): the work done by the machine, equal to the End Load multiplied per the relative displacement (namely equal in both, as depth is angle-dependent), is finally similar for FEA and experimental case.

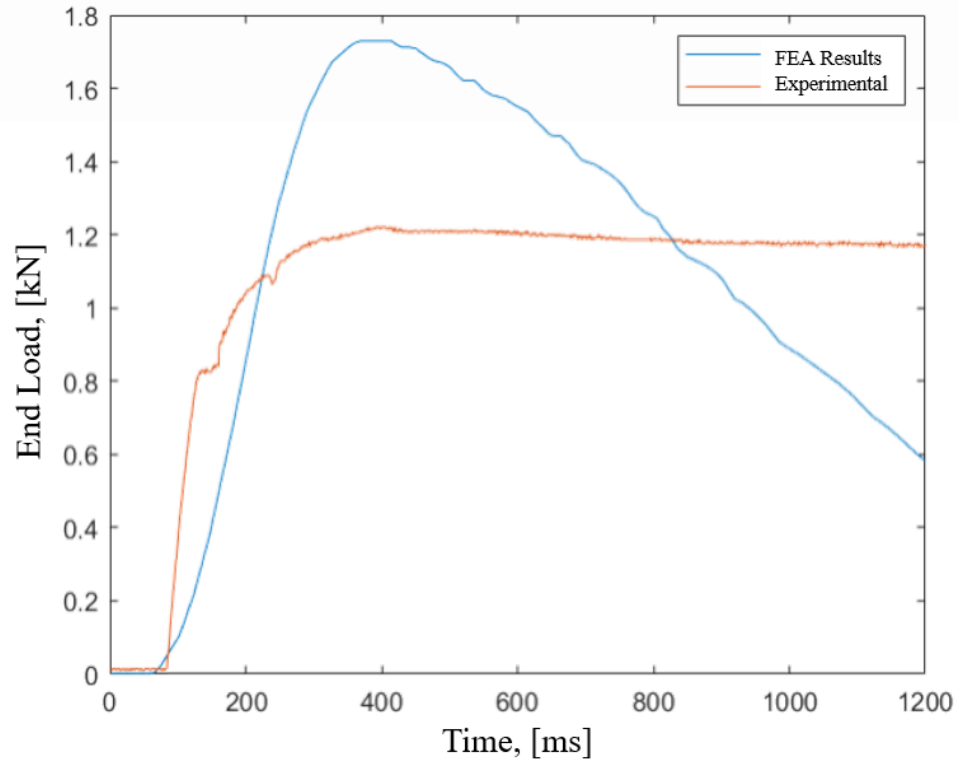


Figure 26. FEA versus experimental End Load.

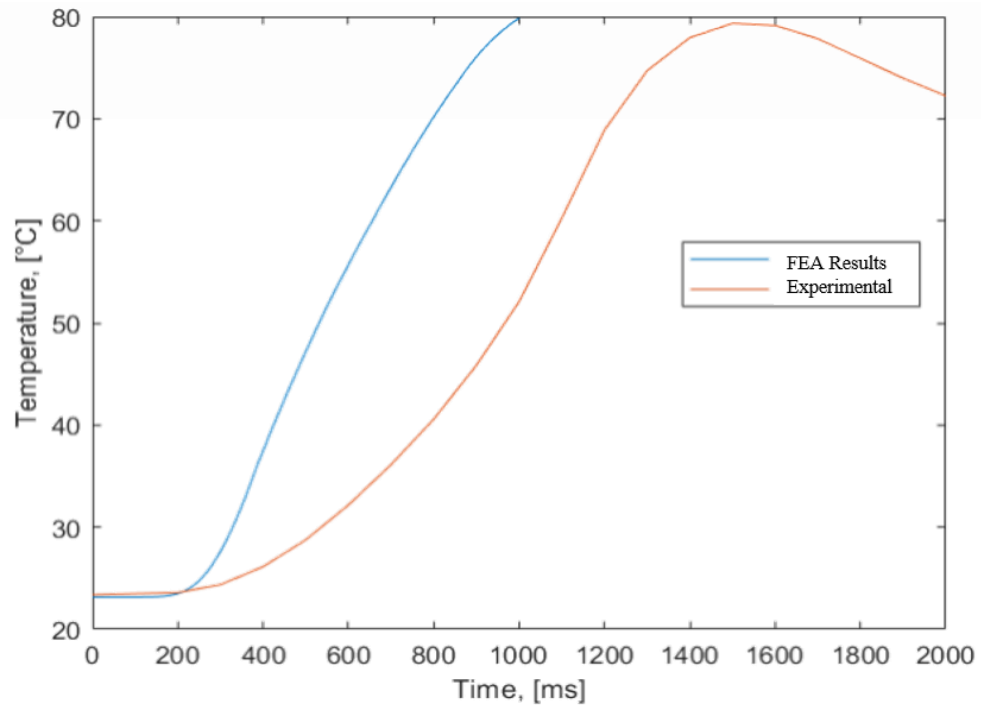


Figure 27. FEA versus experimental temperature.

Considering Figure 27, the different temperature trend is evident: whereas the peak values are very close to each other, at first the heat propagation is more gradual in reality, while the increasing trend is similar. Moreover, the decreasing trend is not registered in the numerical simulation, as the curve tends only to a peak without overcoming its maximum value. This discrepancy is to be traced back to

- The workpiece' dimensions, which have been reduced from those exposed in Figure 11 up to a disk of radius = 10 mm, in order to limit the Computational Time (fewer elements to be considered).
- The thermocouples measurement being taken during the whole process, whereas only the piercing phase is simulated.

To validate the former statement, a temperature comparison for a 1 second process with a workpiece having radius = 15 mm has been performed, with the results in Figure 28: the increasing trend is importantly diminished, as well as the peak temperature is; as said before, this fact is coupled with the different conditions in which measures were taken, with FEA ones referring only to a part of the whole process (as instead was traced in reality by the thermocouples).

In considering the material itself, the maximum temperature value is intended as the limit for comparison between reality and numerical modelling, and in these “successful” runs it has proved valid within a 10% threshold, necessary to comply with the drawbacks of the simplifying hypotheses previously exposed.

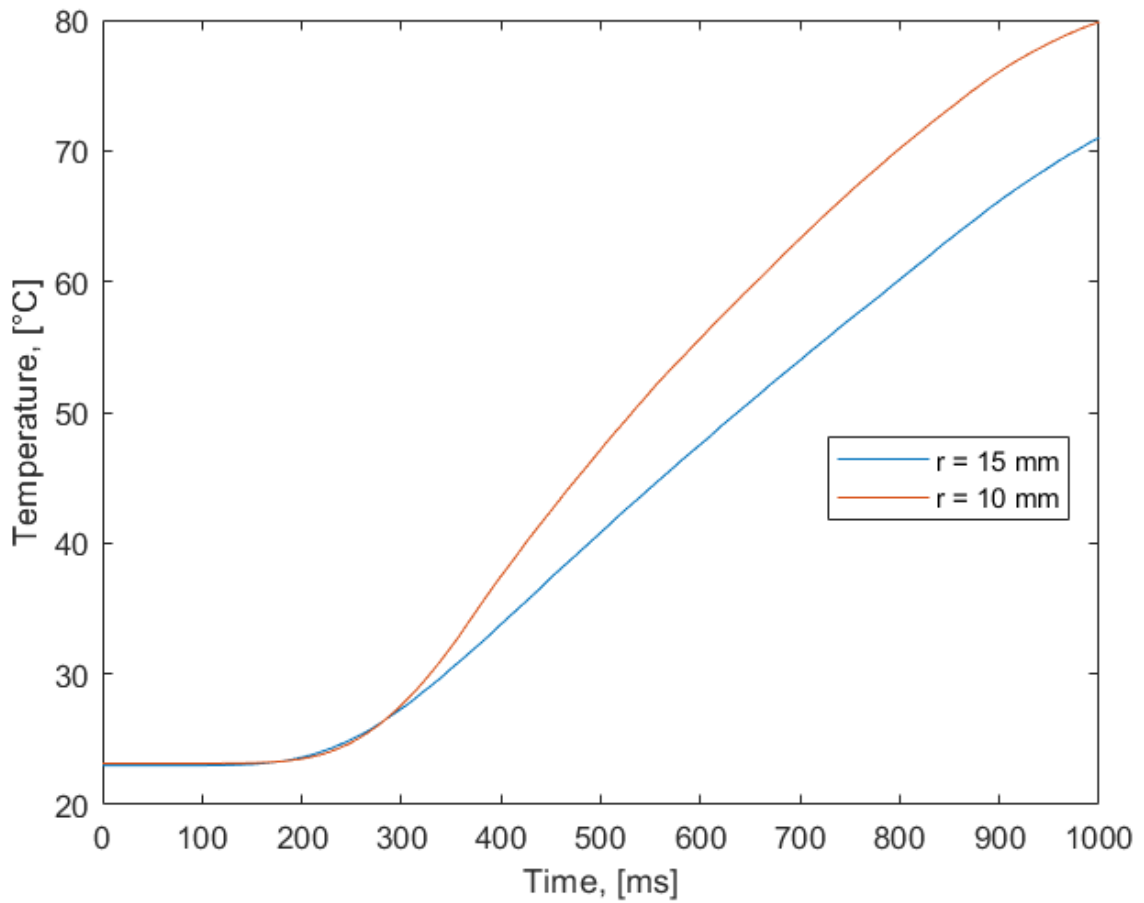


Figure 28. Standard vs. expanded specimen' FEA temperature.

To conclude the part related to the FEA simulation results, the Equivalent Stress distribution inside the workpiece is presented (Figure 29): by reporting the elements surrounding the lower sheet, one can understand the causes behind some regions of higher stress arising at point of first contact between the sheet and the platen, as well as between the former and the upper sheet. To avoid punctual stress induced by the

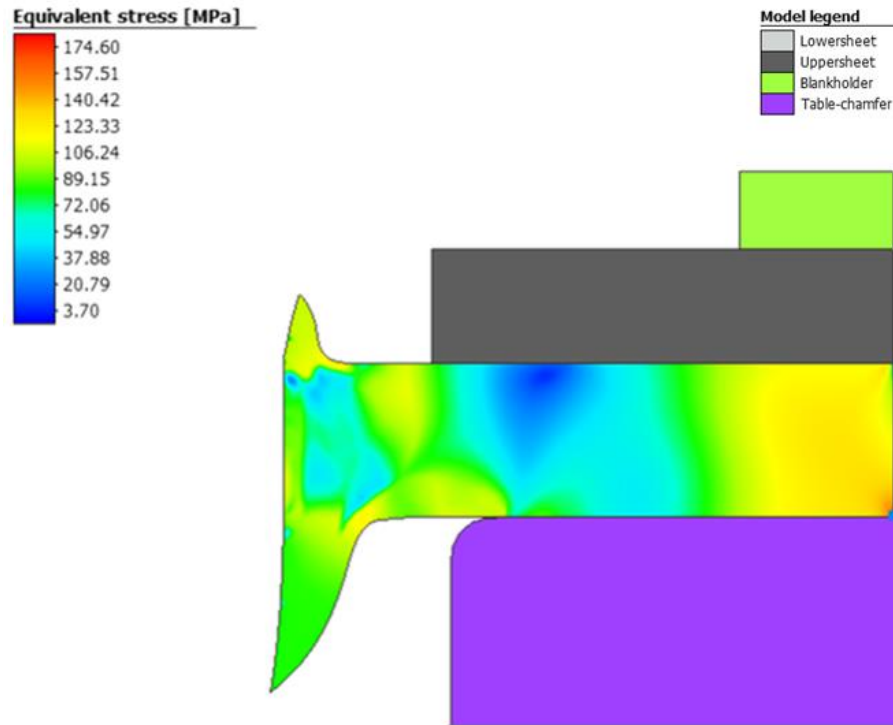


Figure 29. Equivalent Stress distribution in the FEA workpiece.

workpiece bending as the screw penetrates, the sharp edge of the *Table* was substituted with a wide fillet having radius = 1 mm. The maximum Equivalent stress is reached at the workpiece' lower extremity: it is dictated by the boundary conditions imposed to the simulation, as well as by the truncation of the whole simulated assembly pointed at reducing Computational Time, but it is still well below the AW6082-T6 Yield Strength (minimum of 200 MPa, see Table 4). Now looking at the workpiece zone involved in Piercing, you can notice that the Equivalent stress is higher at the surface bending, in the transitions between the plane surface and the extrusions, while in the extrusions themselves the material plasticity during screw penetration, induced by frictional heat, implies lower and more uniform stress conditions.

Now looking at the Factorial study, for every output (*Perc*, *L1* and *L2*) the Main Effects Plot is presented together with Pareto chart of standardized effects:

- The former is adopted to estimate the effect on a single output of each factor, in comparison with its mean value.
- The latter is necessary to understand which factors have the largest effect on the response; moreover, a reference line is used to indicate which ones are statistically significant.

In Table 10 all the combinations derived from the DoE analysis are shown. Following, each output is analyzed in detail. In the last paragraph, referring to Figure 33, the response optimization is presented, remembering to remove the Center point from the analysis as required by the data analysis software itself.

Table 10. Combination for each Factorial analysis' run.

| Run ID | SF_0 | SF_Melt | mu | m | rpm |
|--------|------|---------|------|-----|------|
| 1 | 0.1 | 0.1 | 0.1 | 0.4 | 8000 |
| 2 | 0.1 | 0.1 | 0.1 | 0.2 | 6000 |
| 3 | 0.1 | 0.2 | 0.1 | 0.2 | 8000 |
| 4 | 0.2 | 0.2 | 0.1 | 0.4 | 6000 |
| 5 | 0.1 | 0.1 | 0.4 | 0.4 | 6000 |
| 6 | 0.2 | 0.1 | 0.4 | 0.2 | 8000 |
| 7 | 0.1 | 0.2 | 0.4 | 0.2 | 6000 |
| 8 | 0.2 | 0.2 | 0.4 | 0.4 | 6000 |
| 9 | 0.15 | 0.15 | 0.25 | 0.3 | 7000 |

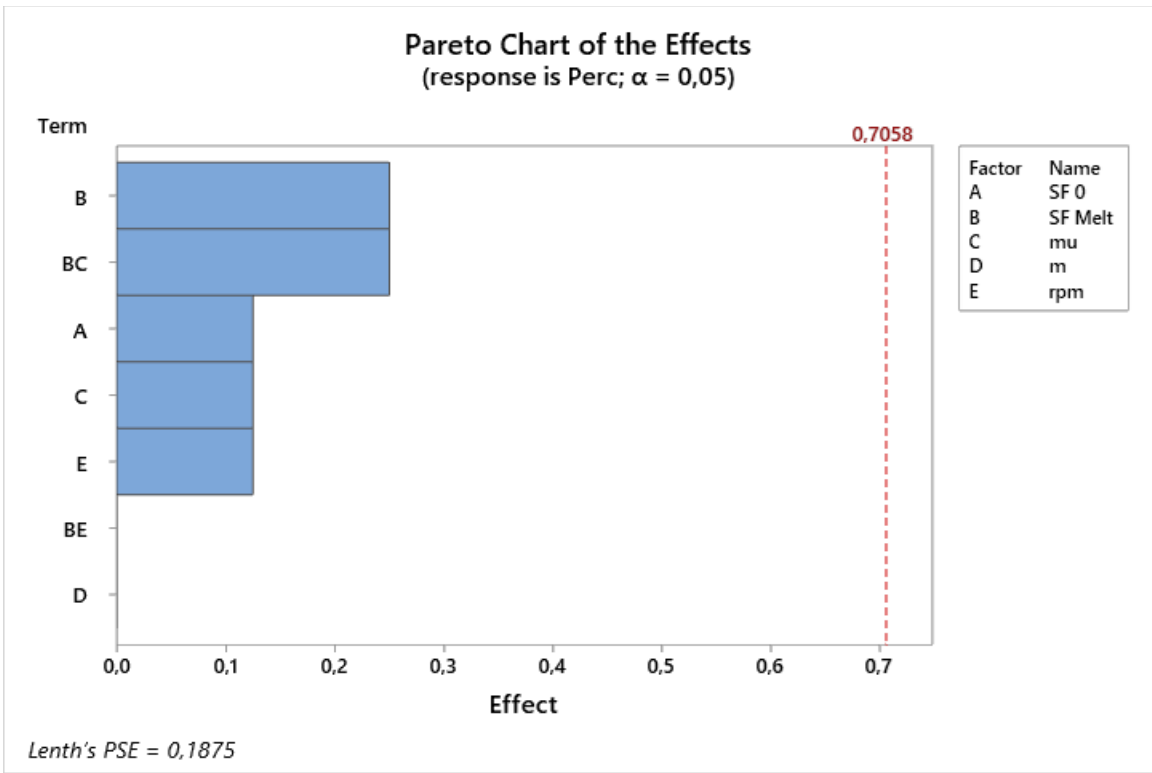
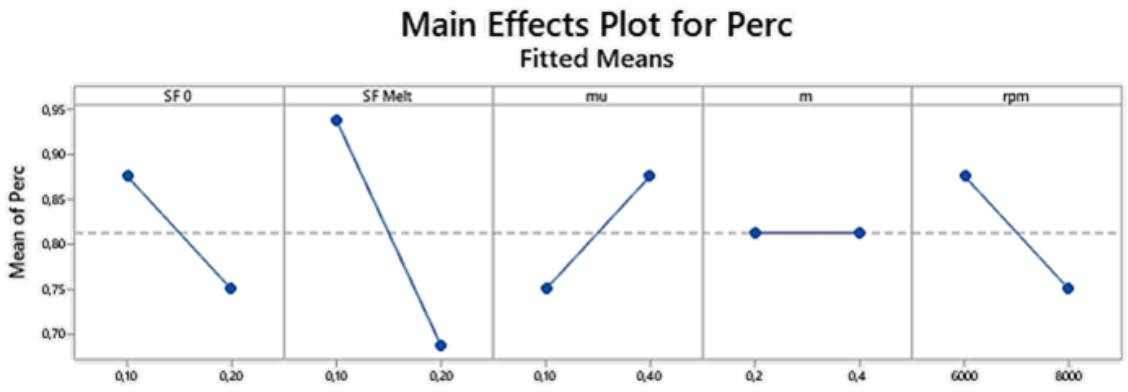


Figure 30. Main Effects Plot and Pareto Chart for *Perc* response.

As clearly expressed in Figure 30, the influence of all factors on the *Perc* response is firmly stated as “statistically not significant” by the Pareto Chart: only the Scaling Factor at Melting Point, and its combined effect with Coulomb friction coefficient are slightly standing out compared to Scaling Factor at 0°C, Coulomb μ alone and screw rotational speed, while Interface shear factor and SF_Melt combined with rpm have negligible weight. The Pareto Chart is necessary to understand whether the dependance between a factor and the output value is statistically confirmed or not (as in the Main Effect Plot). In terms of factors effect on *Perc*,

- Both lower SF_0 and SF_Melt lead to higher probability of FEA simulation success; this trend is confirmed up to “minimum values” (lower than 0.1) through the heatmap reported in Figure 22.
- Higher Coulomb friction coefficient μ increases *Perc*; moreover, the 0.4 value is close to the one chosen as maximum in combined Stick Slip contact conditions.
- Interface shear factor m seems uninfluential (thus at first justifying the range available for its selection for friction law at workpiece-screw contact).
- Lower rotational speed leads to fewer defects (and so, failures) possibilities, as also evidenced in reality (see defects list in Chapter 1.1).

In the Pareto Chart, the α (alpha) term stands for the significance level, that is, the probability of assessing a significance case when there is not; the 5% value assumed is widely adopted and recognized in the industrial environment, and it directly influences the statistical significance of each factor that has been discussed before.

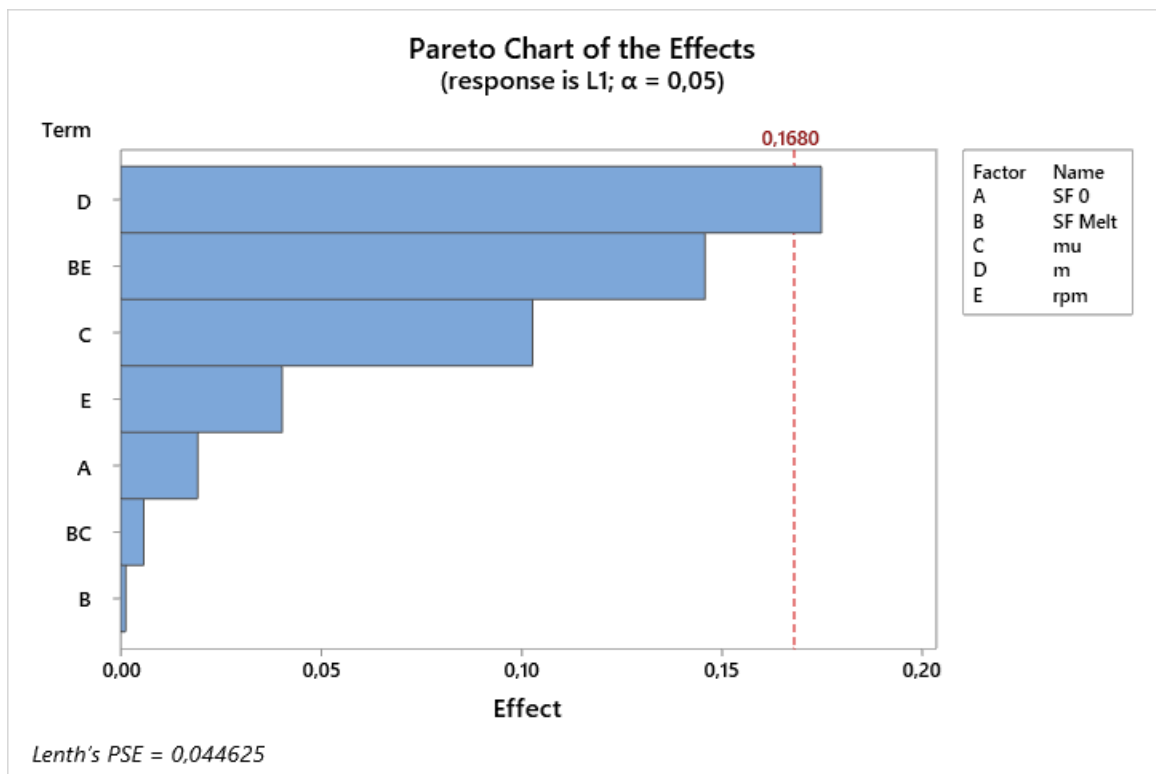
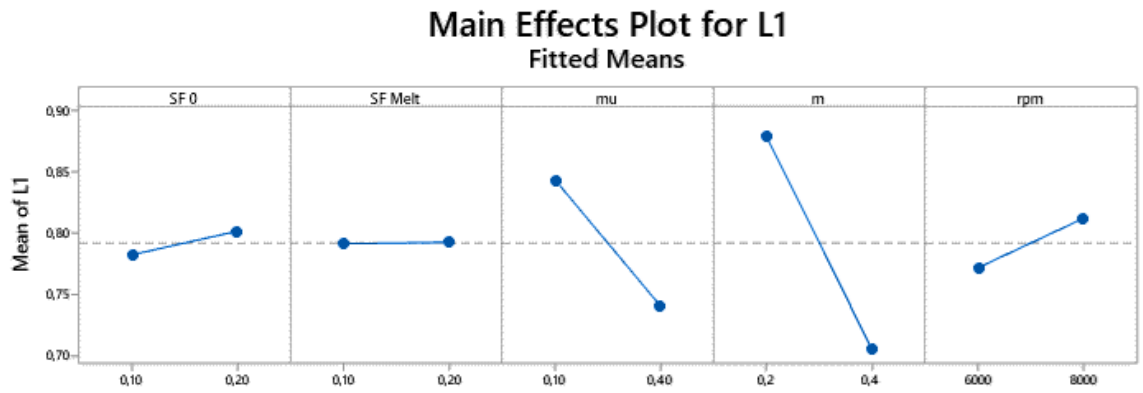


Figure 31. Main Effects Plot and Pareto Chart for *L1* response.

In the case of output LI , from Figure 31 you can notice that Interface shear factor m is the only factor statistically significant, i.e., having a marked effect on that height. Next, the interaction between Scaling Factor at Melting and screw rotational speed is slightly under the significance threshold, followed respectively by Coulomb μ , rotational speed alone, SF_0, combined (interaction) effect of SF_Melt and μ , and finally SF_Melt alone. Now looking at the Main Effect Plot, it can be said that

- Scaling Factors have only marginal effect on LI , with just SF_0 increase directly involving it; this was deduced also in all the numerical simulations performed, in which SF influenced mainly $Perc$.
- Both the friction coefficients' increases lead to the upper extrusion' height decreasing, with m being more influent than μ ; this could be caused by the material becoming more deformable due to its higher plasticity, which is at its time in strict relation with frictional heat.
- Rpm's increase slightly increases LI ; the factor was seen more influential on $Perc$.

At last, looking at the Pareto Chart in Figure 32, which is dedicated to the sensibility study on L2, the heaviest effect (even though far from being statistically significant) is the Coulomb friction coefficient, followed in order by Interface shear factor (closely), SF_Melt combined with rpm, then with μ , next SF_0, rpm alone and lastly SF_Melt. The same dependencies of LI are traced in the Main Effect Plot for the Scaling Factors; both Coulomb and Interface shear coefficients increase leads to that height increase, while rpm remotely possesses a direct dependance with it.

All the factors' effects for each response are presented in Table 11.

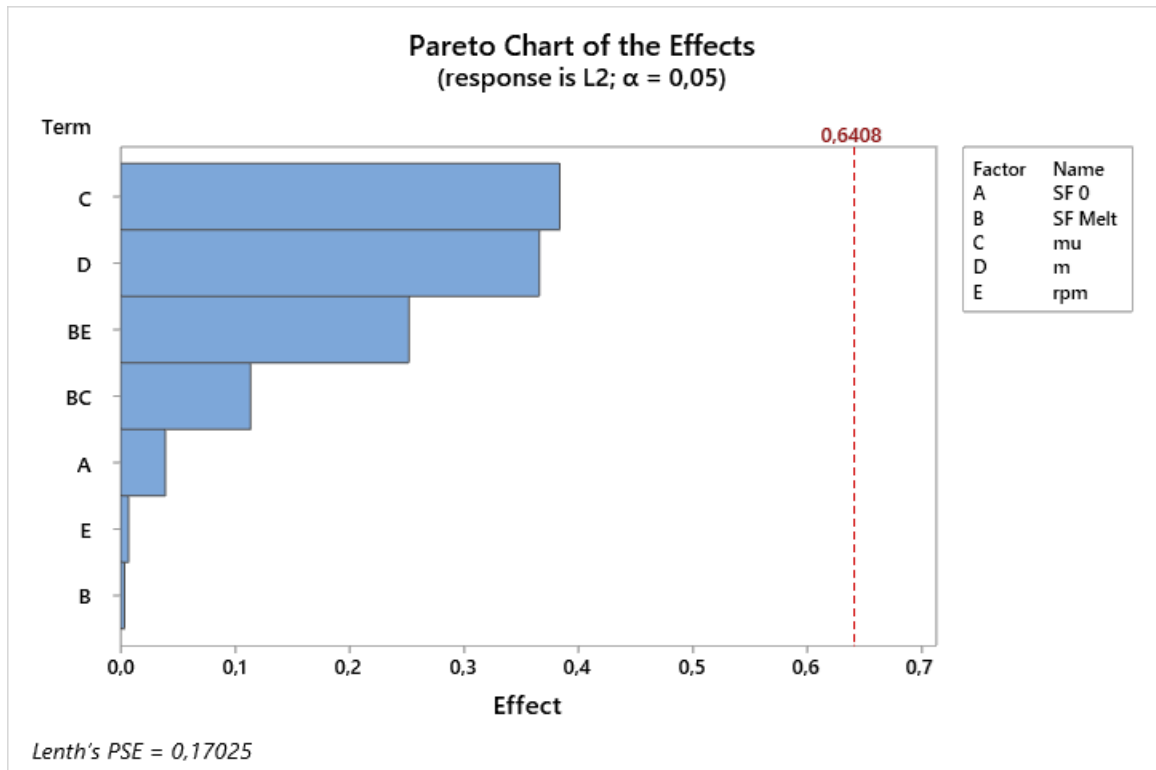
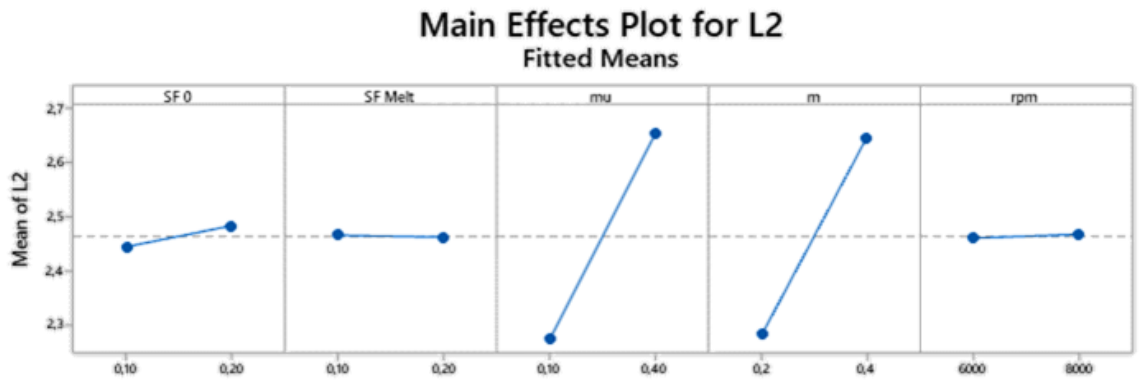


Figure 32. Main Effects Plot and Pareto Chart for L_2 response.

Table 11. Summary of factors' effect on each output.

| Factor | Effect on <i>Perc</i> | Effect on <i>L1</i> | Effect on <i>L2</i> |
|---|---|---|---|
|  Scaling Factor at 0°C |  |  |  |
|  Scaling Factor at Melting |  |  |  |
|  Coulomb μ |  |  |  |
|  Interface shear m |  |  |  |
|  Screw rpm |  |  |  |

As outlined before, inside Minitab environment there is the possibility for Response Optimization: by inputting the desired behavior for each response (namely, *Minimize*, *Maximize*, *Target Value* or even *Do not optimize*), the software statistically determines which is the factor values' combination that will most likely lead to the optimal set conditions. For this research, all *Target Values* were chosen, with *Perc* pointed to 1, *L1* and *L2* respectively to 0.95 mm and 2.3 mm (as on average observed in real extrusions). The complete optimization is shown in Figure 33.

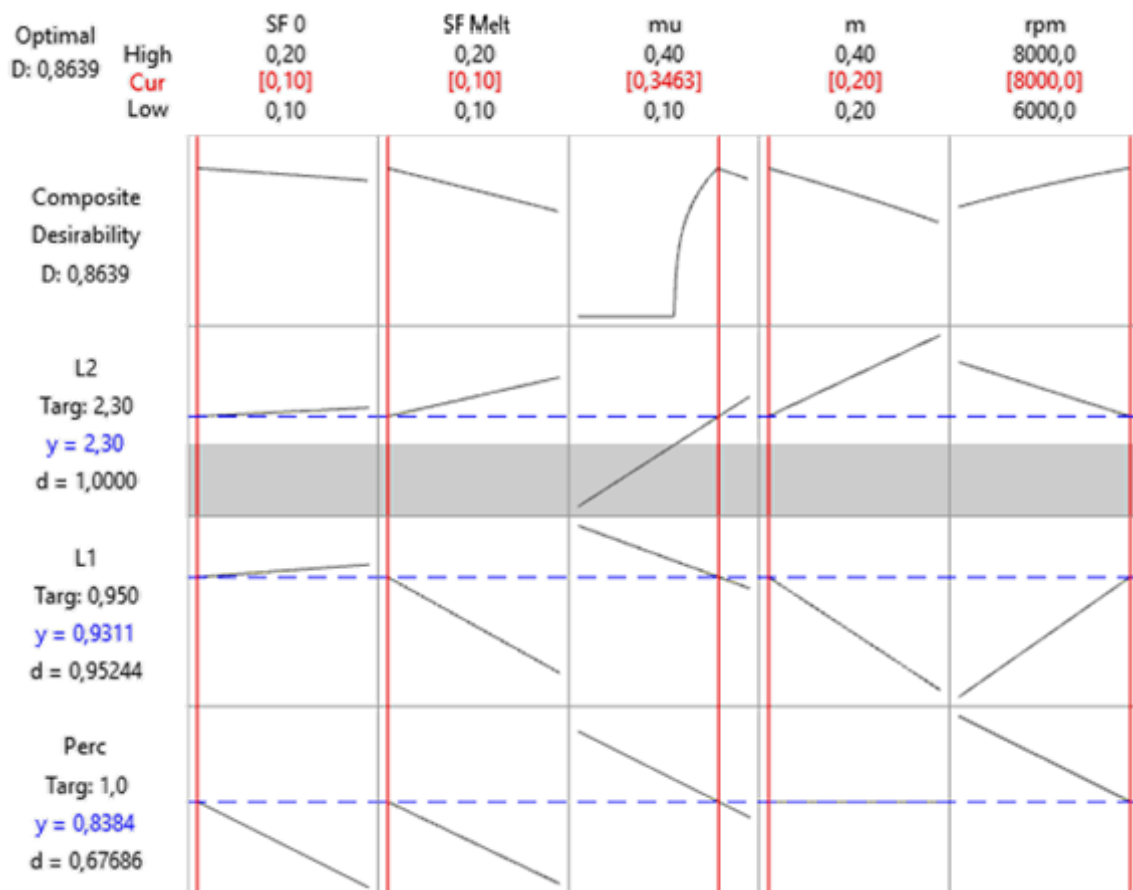


Figure 33. Response Optimization for *Perc*, *L1* and *L2*.

The diagram shown in Figure 33 must be read associated to the following scheme:

- In the upmost region, the factors' range is presented in terms of “High” versus “Low” values, with the optimized one in red characters; in this attempt, the combination A=0.1, B=0.1, C=0.346, D=0.2 and E=8000 was calculated by the software, and the values are clearly justified from the results exposed in Table 11.
- In the left column of the table, the Composite Desirability D is calculated equal to 0.864 (that is, there is around 86% probability of the FEA run converging to the desired outputs for the optimized combination). It is computed as the weighted geometric mean of the desirability d of each response, which in turn indicates the likelihood of reaching the target. Eventually, for each output the *Target Value* is posed in relation with the probable simulated one.
- In the central part of the table, all the graphs with the FEA simulated trends of each response in relation with each factor variation are depicted; for each response, the dashed blue line represents the *Target Value*; at the level of D, the sum of each response trend, mediated with its own d, is computed, in order to define the factor value at the highest D (seen in correspondence of the vertical red line crossing the blue dashed one). The gray region means that an out-of-scale value has been reached, which consequently conditions the other trends to a minimum at the Composite Desirability graph.

3.2 Model testing

Now that the main factors have been satisfactorily exposed and their values chosen accordingly to scientific methodology, the 2D case is deepened with the analysis of variances within:

- Software environment, as for rigid versus deformable screw (Figs. 34÷36) and Fracture Criterion (Figs. 37 and 38).
- Contact condition governing the process, i.e., tribological factors (Figs. 39÷42).
- Variables related to the real assembly, identified as different lower sheet's materials (Figs. 43 and 44) and thickness (Fig. 45), and screw rotational speed (Figs.46 and 47).

It is necessary to say that, apart for some numerical model parameters implying important variations of the results (for instance, change in the workpiece material), the material forming software demonstrated good proficiency in results robustness: as even when the simulation encountered computational divergency, the single run' progression step at which the simulation stopped was precisely the same for every further simulation launched with the same initial settings. This “computational reproducibility” was fundamental whenever a comparison between runs was necessary, and, although surely verified for more widespread FEA simulation tools, it is a strong point when employing CAD and Numerical Modelling to reproduce and support experimental testing.

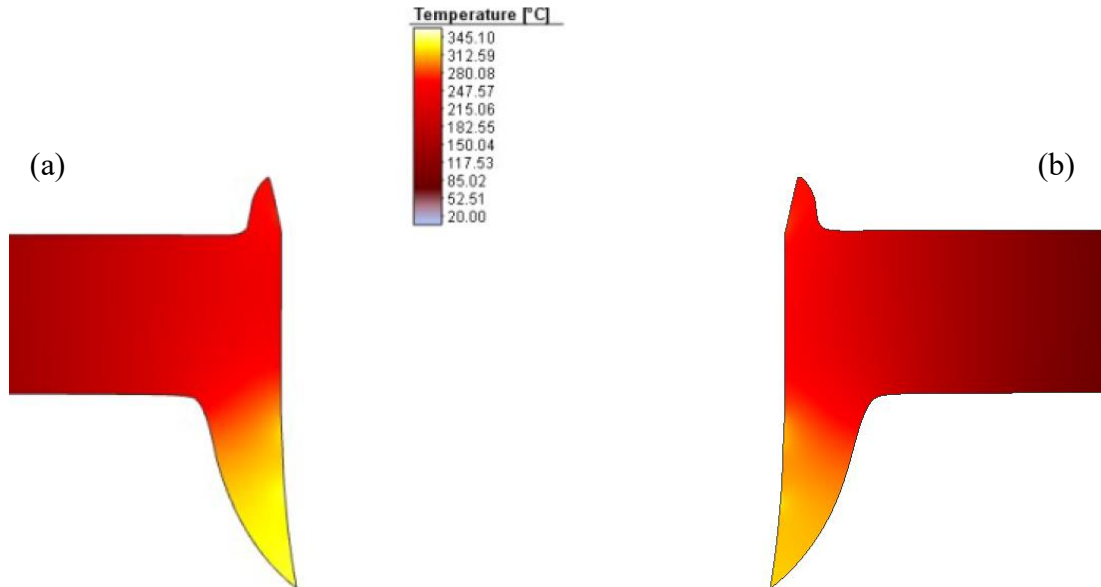


Figure 34. Deformable (a) vs. rigid (b) screw: FEA geometrical and thermal comparison at lower sheet.

From Figure 34, where the final extrusions' shapes for the two considered cases are shown, little to no difference are visible in the numerical simulation results; the only discrepancy is in the temperature field: while the hot-to-cold regions are approximately with the same extension, the peak value for rigid screw is 333 °C, i.e., around 5% lower than for deformable screw. This difference can be explained by the lack of heat generation due to FDS deformation and wear that characterizes the first case.

From Figure 35 one can understand which are the real differences when attributing “rigid with heat conduction” condition to an element: the screw' portion in Fig. 35b presents heat diffusion inside (this is not possible for the “rigid” condition of Fig. 35a), but lacks the tip wear which, even though minimal, is present on the left (Fig. 35b).

Finally, the former' temperature is around 30% higher than the latter', fact also in this instance related to absence of energy dissipation by material deformation.

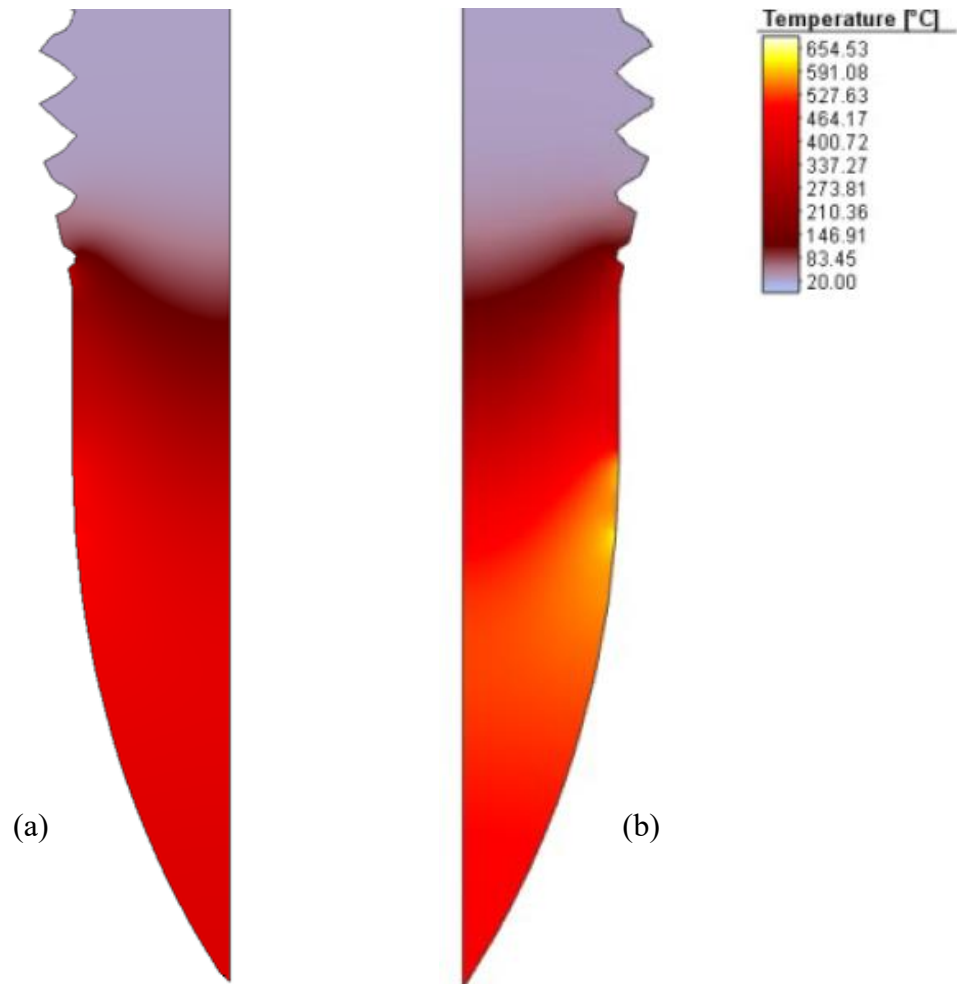


Figure 35. Deformable (a) vs. rigid (b) screw: FEA geometrical and thermal comparison at screw.

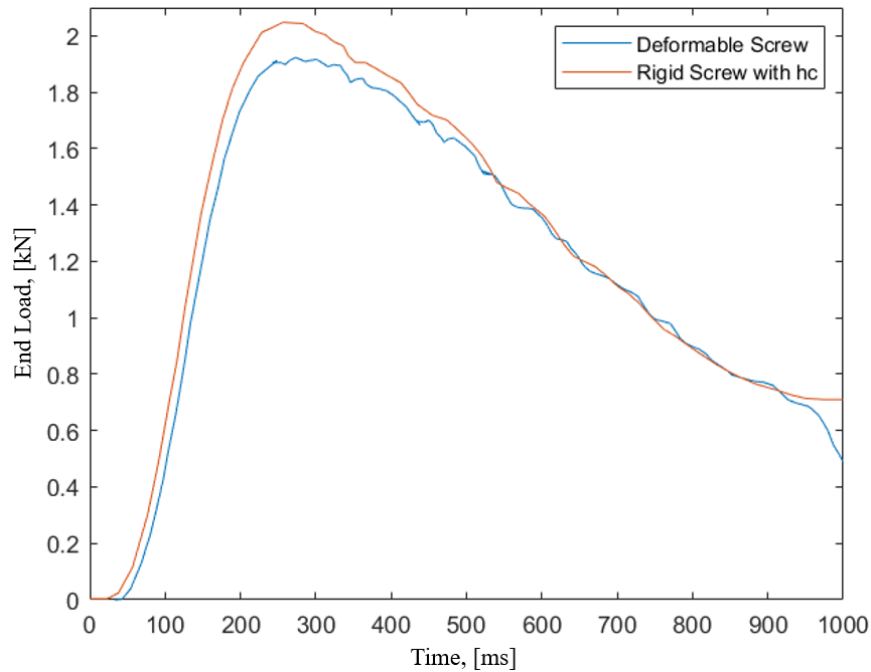


Figure 36. Deformable vs. rigid screw: exerted End Load from FEA.

From Figure 36, another important aspect of rigid versus deformable screw is analyzed: the axial force applied by the Weber machine to perform piercing. In the case of deformable screw, the max value is under the 2 kN threshold (and so, respecting “Pass” criteria), and the decreasing trend (on the right of the diagram) is characterized by oscillations, significantly related to the FDS tip’ surface wear. On the other hand, in the case of rigid screw with heat conduction the pushing phase starts before (no tip flattening in-between), reaches a maximum value > 2 kN and has a smoother decrease, although ending at 40% higher axial force with respect to the one registered in the other condition. Concluding, the rigid screw model results to be less accurate and thus not recommended, as leading to discrepancies in End Load evaluation while only providing a benefit of around 15% in reduced Computational Time.

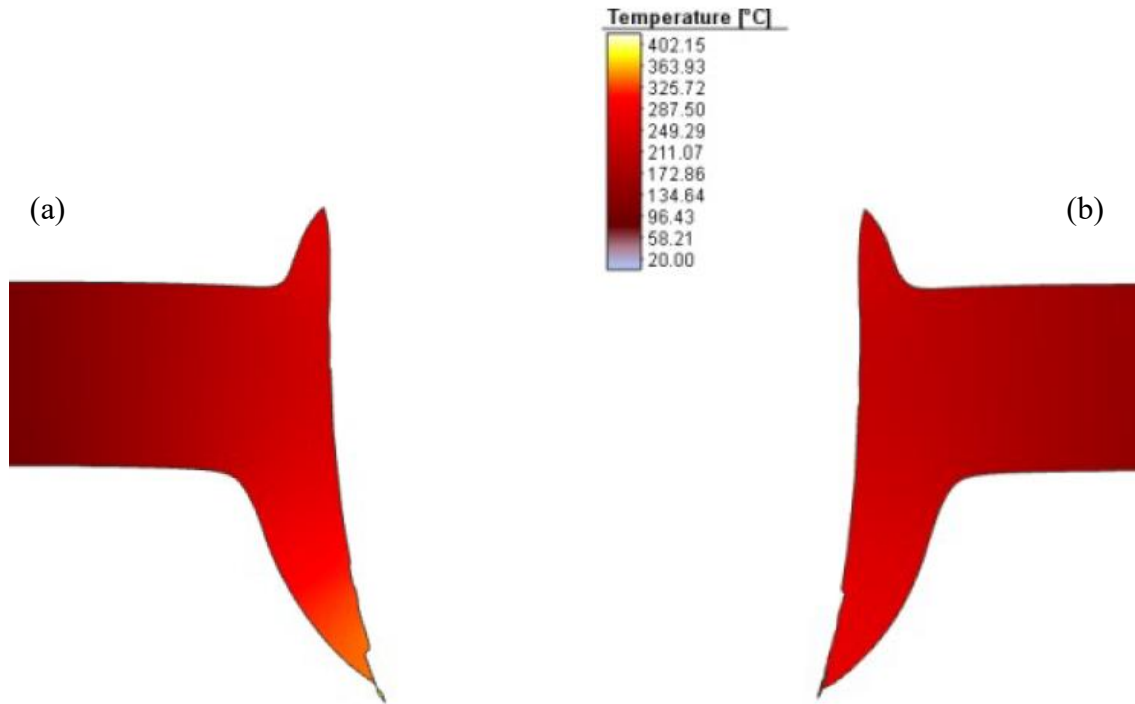


Figure 37. Without (a) and with (b) damage criterion: FEA geometrical and thermal comparison at lower sheet.

Now, let's consider the Fracture Criterion (FC). As from [18], two parameters were required for the normalized Cockcroft-Latham Model: the nCL, seen in Eq.11, and the Element Deletion percentage, that is the percentage of nCL at which a mesh element is admissible to deletion due to damage. As it is evident in Figure 37, little to no difference is present in terms of temperature field, with only a peak registered in the FEA simulation without FC at the chip formation (as said, this is attributable to computational errors); regarding the geometries too, the extrusions height is approximately the same, as for their maximum thickness. What counts is the failure error, which is different: adhesion and material self-intrusion for the former, chip formation and detachment for the latter, as clearly visible in the zoomed views of Figure 38.

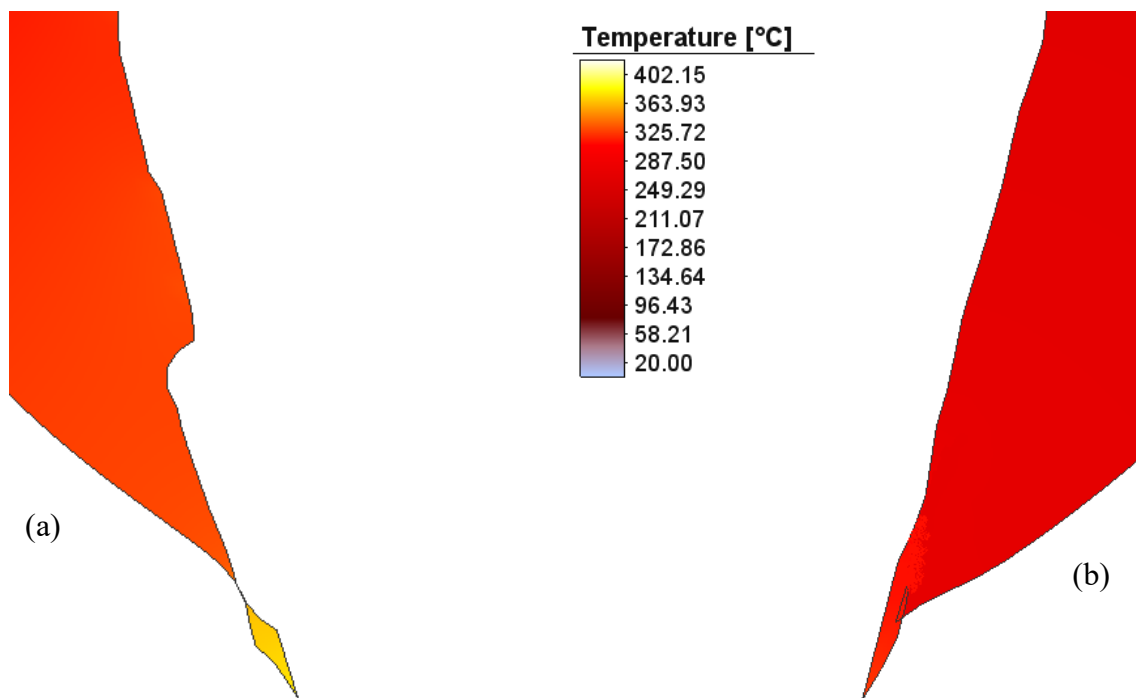


Figure 38. Without (a) and with (b) damage criterion: effect on lower sheet' extrusions in FEA model.

Even if not affecting the applied End Load values, the failure mode is crucial to understand the possible cause of assembling errors: when the FEA results present chip formation, it is said that only real causes, namely rotational speed and axial force, play a role, and so the former must be reduced, whilst the latter increased; on the other hand, adhesion to the screw and self-intrusions in the simulations can be controlled only by in-software tools (a.i., within the *Contact Table*). In summary, the introduction of the FC in FEA allows to verify whereas the error is simply computational, or if real conditions cause unfeasibility in joint assembling.

In terms of tribological analysis, the research pointed at comparing the well-known Skovron-based combined Stick-Slip contact condition with other models already adopted in the Literature: the combinations are exposed in Table 12, the juxtaposition between other friction laws and coefficients comes after. As said, the chosen combinations have been determined from already-presented studies in the hole drilling field, and mainly for series-6000 Aluminum alloys in contact with Dual-Phase Steel. Further numerical simulations with similar conditions were run, only changing the values of the coefficients, but the author rather preferred to present a sum-up of the most significant findings.

Table 12. Friction Laws and coefficients combination of the tribological analysis.

| Denomination | Coulomb friction coefficient μ | Interface shear factor m |
|--------------------------|---|----------------------------|
| Combined Stick-Slip, [6] | Temperature-dependent, see Figure 19 | Constant, 0.2 |
| Mixed Coul-Shear, [17] | Constant, 0.1 | Constant, 0.2 |
| Coulomb only, [10] | Constant, 0.15 | / |
| Shear only, [19] | / | Constant, 0.9 |

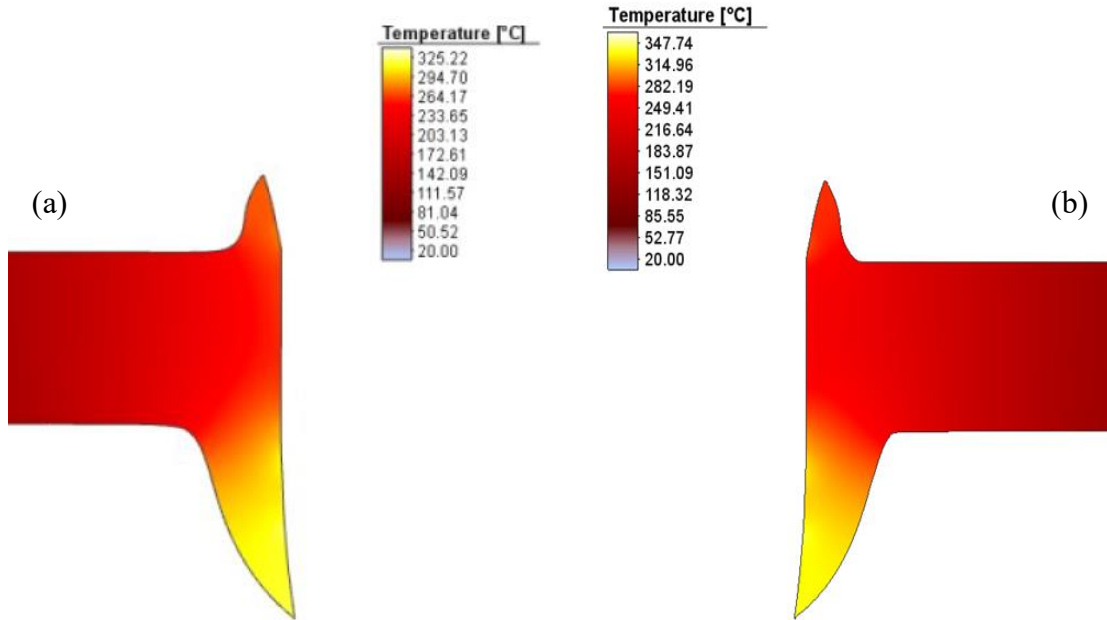


Figure 39. Combined Stick-Slip (a) vs. Mixed Coul-Shear (b): FEA geometrical and thermal comparison of extrusions.

As first step, the friction law derived from the combined Stick-Slip contact condition [6] is compared to the Mixed Coulomb-Shear law, as exposed in [17]; as said, the former law integrates Coulomb' coefficient μ seen in Figure 19 with Interface shear factor $m = 0.2$, as resulted from the Factorial study and validated in the [17]. Looking at Figure 39 at a first glance, the extrusion shapes are similar:

- The petal (i.e., the upper part of the extrusion constituting the boss) has approximately the same height but is bulkier in the Combined Stick-Slip than in the Mixed Coul-Shear. In Fig. 39a it can be also noted a more gradual transition to the workpiece' upper surface while in Fig. 39b there is not a completely “rounded” fillet.

- Regarding the lower part of the extrusion, as for the petal comparison, the former (Fig. 39a) is slightly shorter but thicker in comparison with the latter (Fig. 39b), as well as with better “transition region”.

In order to better comment the extrusion dimensions, in Table 13 the most important data from numerical analysis are reported and compared to the experimental ones, obtained as mean values of P41, P42 and P44 piercing experiments. As previously expressed, the experimental tests encountered partial thread forming due to difficulties in precisely setting the assembling machine stop, so that part of the material was translated from the lower part of the extrusion to the upper part, giving rise to the possible discrepancies between simulated and real cases.

Considering now the temperature range, the fields are very similar, with the only difference of higher petal’ temperature for the Combined model with respect to the Mixed one; the peak values are around 325 °C for the former, and 350 °C for the latter.

Table 13. Important workpiece quotes: Combined Stick-Slip vs. Mixed Coul-Shear vs. average experimental evidence.

| Dimension | Combined Stick-Slip | Mixed Coul-Shear | Experimental |
|---------------------------|---------------------|------------------|--------------|
| <i>L1</i> | 0.91 | 0.975 | 0.95 |
| <i>L2</i> | 2.295 | 2.225 | 2.3 |
| Max upper extr. thickness | 0.58 | 0.675 | 0.75 |
| Max lower extr. thickness | 0.9 | 0.95 | 0.7 |

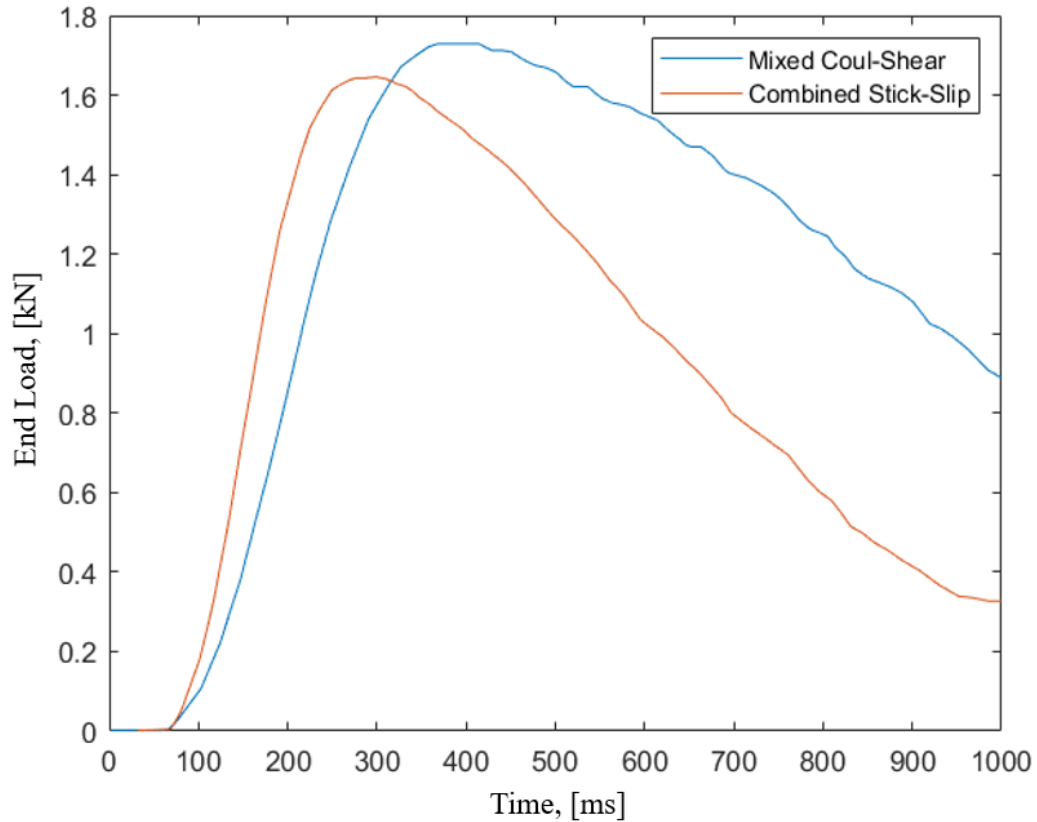


Figure 40. F_z in FEA, Combined Stick-Slip(a) vs. Mixed Coul-Shear(b).

To conclude this comparison, the axial force applied in piercing is reported in Figure 40: as the Mixed Coul-Shear generates minor frictional heat while in normal stress condition ($\mu = 0.1$ compared to minimum 0.15 of Zinc-Aluminum Alloy), in the case of the Combined Stick-Slip frictional law the tip penetrates with minor material resistance, and so, faster. The End Load is reduced noticeably after the four lobed tip' section crosses the entire lower sheet, up to reaching a constant value when the cylindrical region of the screw is met (as ideally expected), while the decrease in the former case is more limited, which could imply overall higher work required for this phase, as explained before.

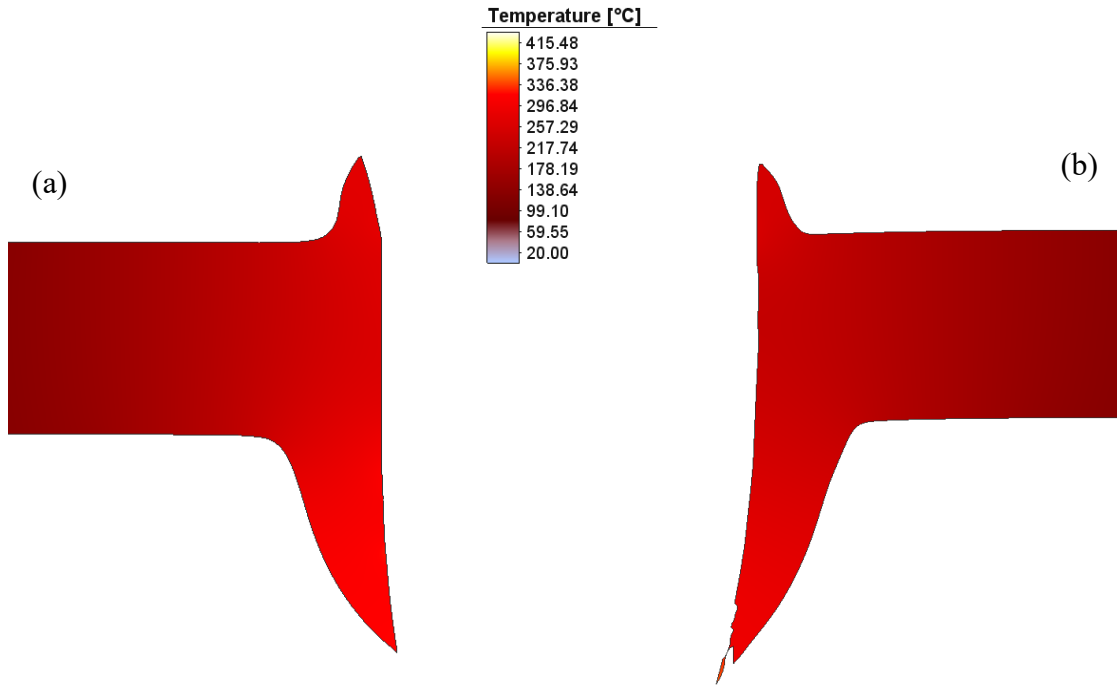


Figure 41. Combined Stick-Slip (a) vs. Coulomb only (b): FEA geometrical and thermal comparison of extrusions.

As result of adopting Coulomb Law only to simulate the piercing phase, the run ended due to non-convergency (exactly at 93%) with evident chip formation (Figure 41b). You can notice that the upper extrusion is thinner and lower than when using the Combined Stick-Slip: although the Factorial analysis said the lower μ , the higher LI , the former numerical simulation does not include the final petal deformation caused by the conical transition region (as in the latter); on the other hand, the lower extrusion is similar for both, except in the adhesion phenomenon.

Concluding, maximum temperature is more than 20% higher in Coulomb only, but it is to be traced back to probable computational errors linked to chip formation. Regarding the End Load applied on the screw, the maximum passes the 2 kN limit, additionally verifying the incorrectness for Piercing tribology' description.

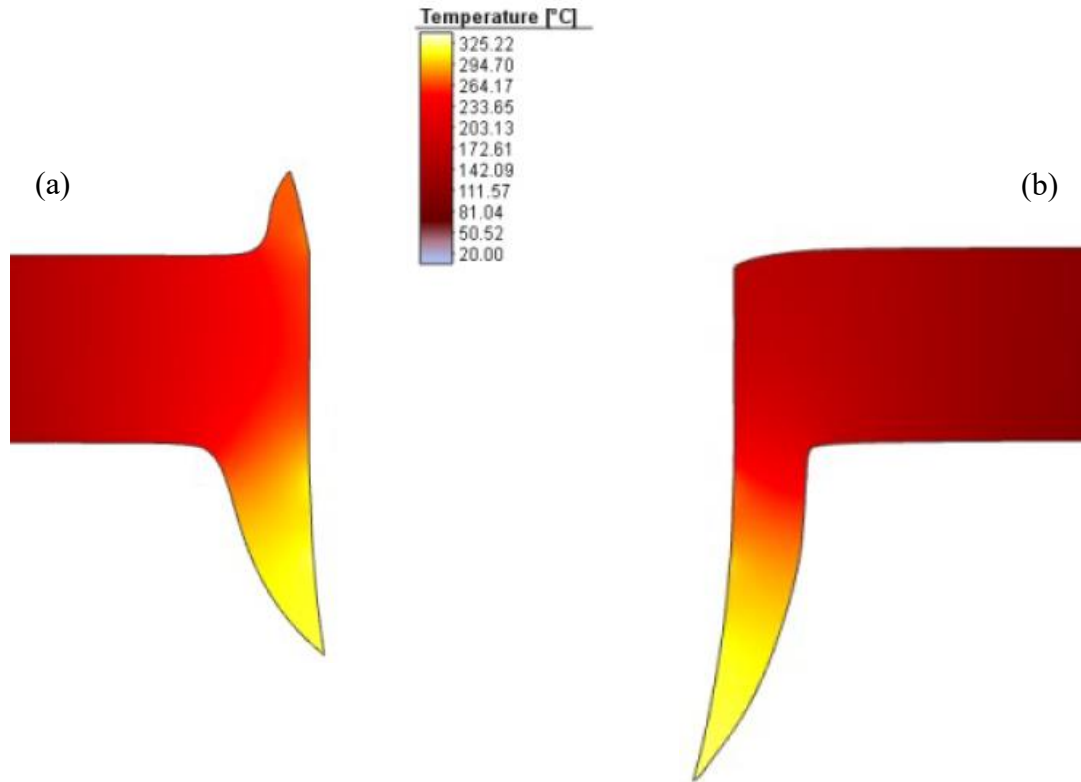


Figure 42. Combined Stick-Slip (a) vs. Shear only (b): FEA geometrical and thermal comparison of extrusions.

In this case, the application of Friction law derived from Literature has led to an extreme case: the upper extrusion, present during the first moments of piercing but already minimal compared to the Combined Stick-Slip one, has been dragged by the screw and, due to the conditions necessarily imposed to avoid material self-intrusion, at last merged with the surrounding workpiece' material due to its thinness. Compared to the Coulomb-only case of Figure 41, you can notice the complete absence of material detachment, probably implied by the plasticity reached by the material, whose temperature is augmented just in the lower extrusion, without valuable increases in the rest of the workpiece.

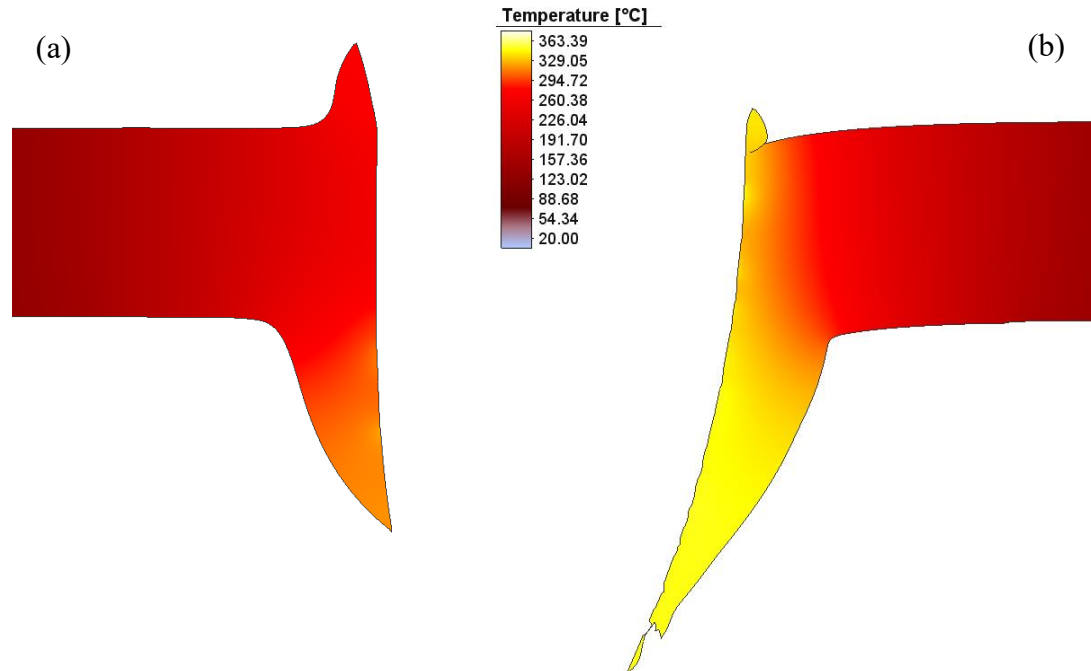


Figure 43. AW6082-T6 (a) vs. AW6061-T6 (b): FEA geometrical and thermal comparison of extrusions.

To conclude the section of 2D axisymmetric piercing centered on Friction and material, the behavior of AW6061-T6 is studied: from Figure 43, the workpiece of the stated material (Fig. 43b) is seen experiencing intense bending, with the surface of contact with the screw encountering adhesion, up to chip formation and consequent run failure (it stopped at 77%); moreover, the upper extrusion' size is minimal, compared to the AW6082-T6 workpiece (Figure 43a), presenting also folding on itself. The main aim of this numerical simulation was evaluating the thermal behavior, strongly in relation with the friction model under use: finally, the temperature demonstrated values within the range (according to [6]) and with similar fields as those encountered in piercing of AW6082-T6. The author is of the opinion that better results could be obtained following

proper Scaling Factor tuning, as well as Interface shear factor evaluation and, probably, with Process Time elongation together with FDS rotational speed reduction; this last sentence is justified by the End Load graph, Figure 44, when considered in its significance zone (i.e., before adhesion takes place - around at 35% increment-), showing peak value almost doubled with respect to those reported in Skovron' research.

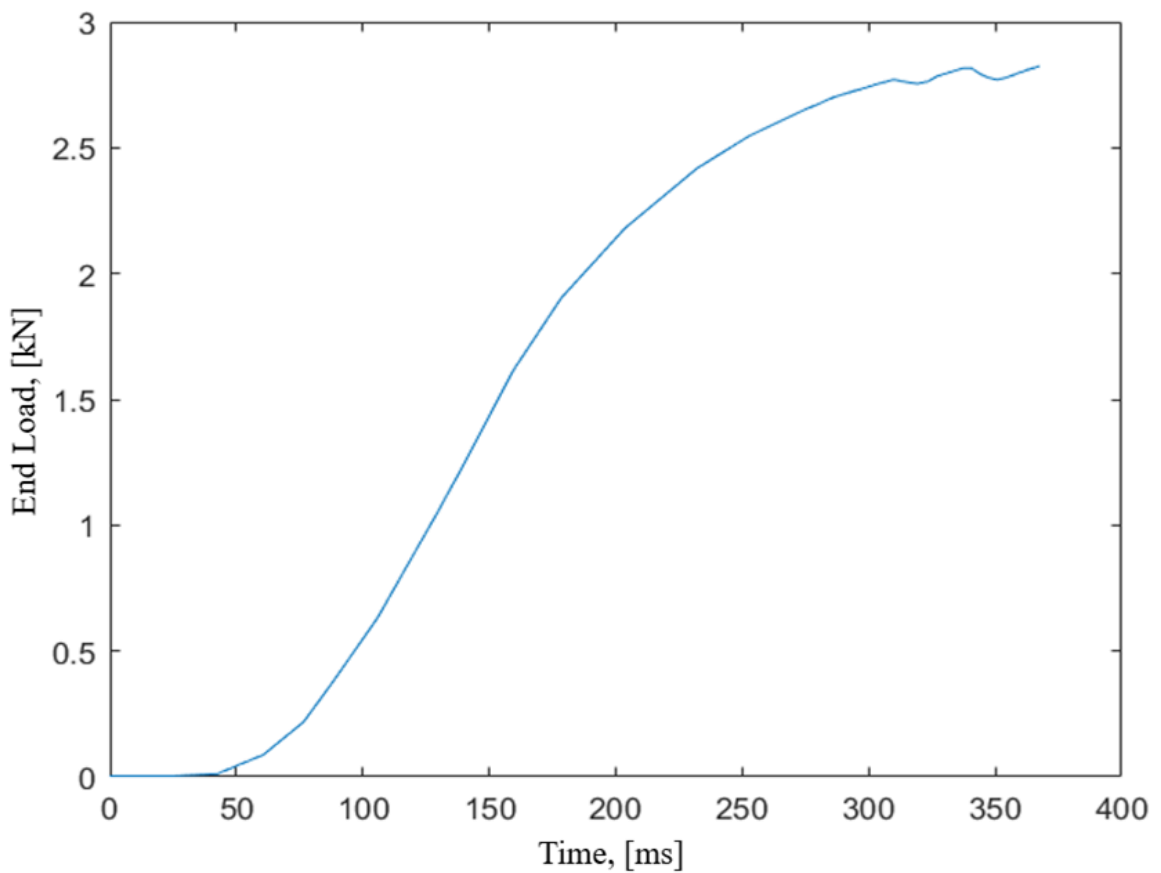


Figure 44. The AW6061-T6 case' End Load graph from FEA.

Another question of interest is the effect of different workpiece thicknesses on the FE simulation outputs. In order to fully answer, at first the 2.0 mm thick extrusions and temperatures are posed in comparison with the 3.0 mm ones, to end up with the effect on assembling applied axial force. The main precaution to be assumed when simulations of different lower sheet thickness are run, are

- Increasing the lower sheet refinement boxes' size.
- Maintaining the screw tip position relatively to the workpiece upper surface.
- Augmenting the Process Time to 1.5 s, as suggested by previous experiments.

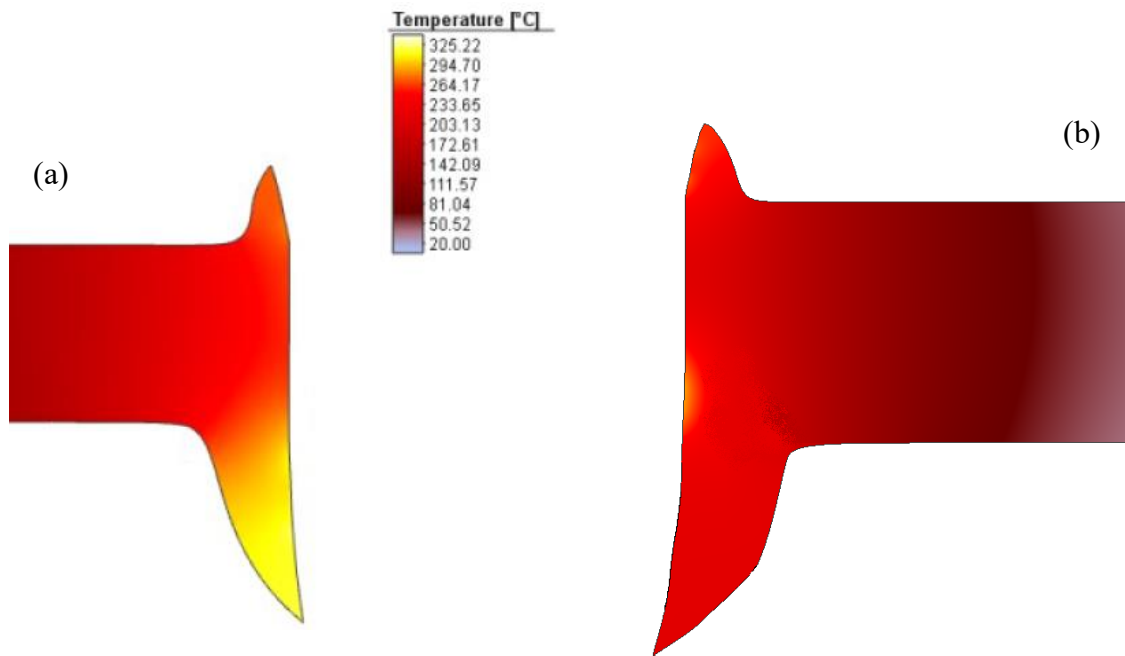


Figure 45. 2.0 mm thick (a) vs. 3.0 mm thick (b): FEA geometrical and thermal comparison of extrusions.

From Figure 45, the main understandings are:

- The material quantity displaced into the boss is noticeably larger for higher thickness; on the other hand, the lower extrusion is shorter in comparison with the 2.0 mm thick corresponding one.
- The upper extrusion maximum width is quite the double than the one of lower thickness workpiece, while the lower extrusion one is approximately proportional. Together with the considerations made at precedent point, and remembering that the screw has the same dimensions in both the runs, you can say that the material tends to be more displaced upwards in this case.
- The peak temperature registered with thicker lower sheet is around 10% higher than that with thinner one, but the ending situation shows an overall cooling, due to larger material quantity present; it can be stated that due to the thicker sheet, the screw frictional work increases, leading to larger material quantity being displaced, which, at its time increasing the total threadable area, allows for more resistant mechanical joints.

Confirming the simulation data, the peak value encountered in the $x = 10$ mm position on the lower surface is 108.3 °C, when the experimentally measured one by using Thermocouples is around 100 °C, so the error is within what stated for acceptability criteria. To conclude, the maximum registered axial force in testing is 1.65 kN, when the value coming from simulations is 2.5 kN: the difference is somewhat 50%, much higher than the allowed one; in this situation increasing the Scaling Factors can help, since augmenting the peak temperatures and, thus, reducing the screw efforts in penetration.

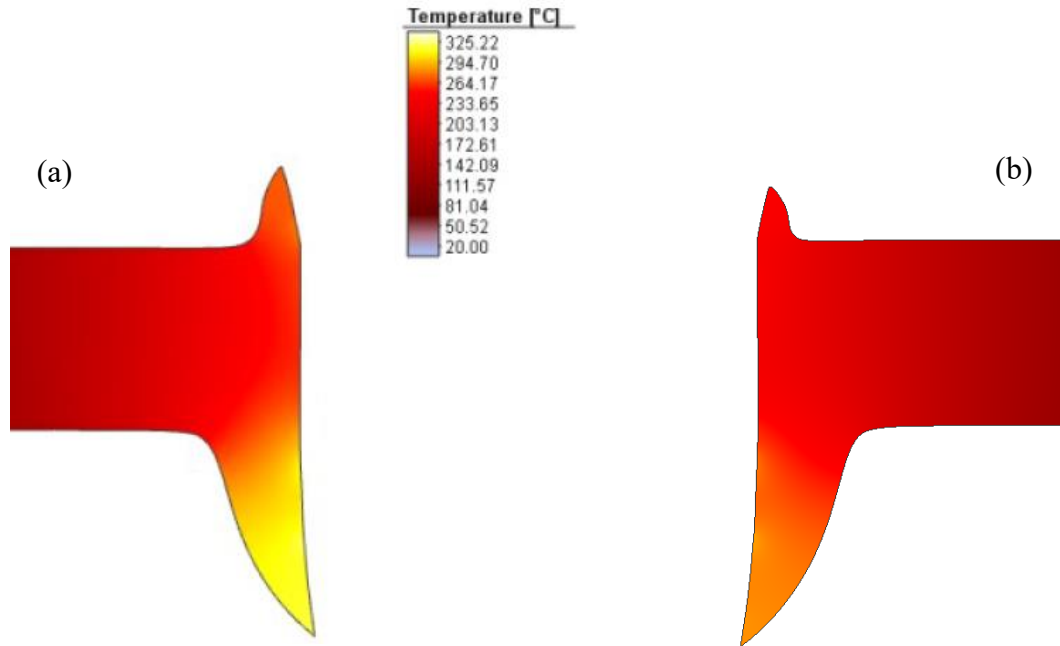


Figure 46. 8000 rpm (a) vs. 5000 rpm (b): FEA geometrical and thermal comparison of extrusions.

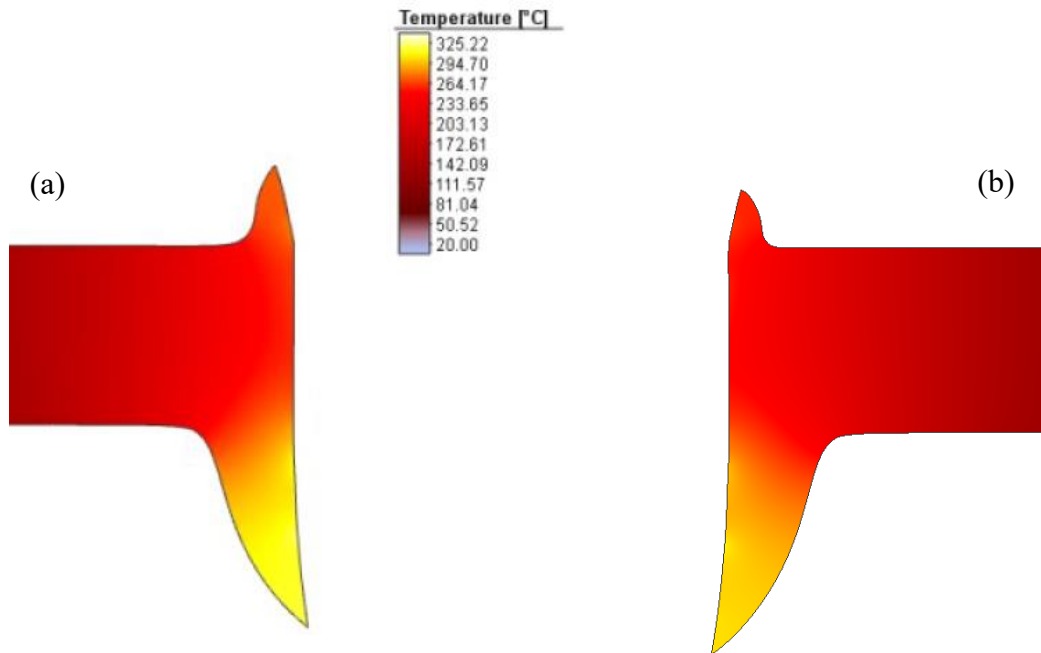


Figure 47. 8000 rpm (a) vs. 6000 rpm (b): FEA geometrical and thermal comparison of extrusions.

From the precedent figures, you can understand that the differences encountered at screw rotational speeds lower than 8000 rpm are marginal: the lower the speed (at constant Process Time), the lower the frictional heat generated, and so lower material plasticity up to smaller material quantity displaced into the petal, as verified in the Factorial study on *L1*. It could be added that having the same SF in all the FE simulations for the same material leads to the same temperature field even for different rpms.

The effect of reduced heat delivered to workpiece is clear also at the axial force applied, as the peaks registered are respectively 2.5 kN for 5000 rpm and 2.3 kN for 6000 rpm: the possible error in acceptability criteria can be avoided with Process Time increment, in order to allow the screw tip more time to penetrate (otherwise, the machine forces the screw' tip into the AW6082-T6 workpiece to respect the 1 s Process Time).

CHAPTER FOUR

CONCLUSION

In this research, the main characteristics of a recent industrial technique for mechanical joining, the Flow Drill Screwdriving, are widely exposed and commented, as well as its physics analyzed in depth. Next, the software Simufact Forming 2020 is used to simulate its piercing phase in 2D, with the fundamental hypothesis of axisymmetry. All the simulation results have been compared with experimental evidences coming from available literature and experimental tests specifically done in the Stellantis Labs of CRF.

In order to develop an accurate FEA simulation of the process, some points came out as fundamentals. They have been the subject of specific attention and careful development in the model preparation. First of all, the characterization of the complex contact existing between screw and workpiece material (AW6082-T6), which has been dealt by adopting the combined Stick-Slip contact condition to reproduce experimental test results on the End Load - Time characteristic curve. Secondly, the Aluminum alloy definition in terms of True Stress-Strain curves has been dealt with the Johnson-Cook model, whose parameters have been experimentally defined starting from the Engineering Stress- Strain curve evaluated in CRF Labs. Among others, the acceptance criteria involved geometrical and physical aspects, as experimentally observed, for instance the lower sheet extrusions' height and the absence of defects related to Piercing, as well as the peak End Load applied by the assembling machine. Eventually, the 2D simulation is successfully developed and optimized, by including in-depth analysis of the Equivalent Stress distribution inside the workpiece .

Successively, many factors supposedly affecting the results are studied: at first, the Scaling Factors at 0°C and at AW6082-T6 Melting Point (650°C) to obtain a valid heat map, then including also Coulomb friction coefficient μ , Interface shear factor m and screw rotational speed in [rpm] all inside a $\frac{1}{4}$ Fractional Factorial analysis. To conclude the piercing phase' research, some comparisons are additionally done on the possible effect on the simulation results of factors such as screw deformation, Failure Criterion introduction for the workpiece, and a tribological study for validation of Skovron combined Stick-Slip contact condition with respect to other frictional laws adopted in similar researches.

Simulation results have been systematically compared with available experimental ones for validation. Particular attention has been devoted to lower sheet thicknesses and screw rotational speeds, in order to reproduce conditions commonly encountered in modern industrial realities.

CHAPTER FIVE

SUGGESTED CONTINUATION WORK

As talking about Flow Drill Screwdriving, the continuation of this research should include Thread Forming and Screw Driving and Fastening. MSC Simufact 2020 software is still a valid instrument, although the results from 2D axisymmetric FE simulations cannot be directly used: due to the spiral shape of the threads, an expansion into Partial 3D (fundamental to save computational resources) of both lower and upper sheets with proper symmetry planes is necessary, as well as complete 3D CAD models for *Table* and *Blank holder*; the mesh and remeshing criteria must be changed, with the suggestion of introducing refinement boxes for the same *Lower sheet* in those areas involved in TF and Screw Driving and Tightening (Figure 48).

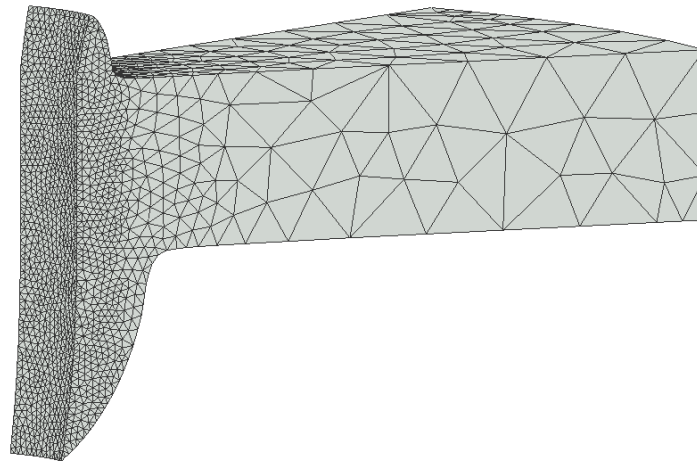


Figure 48. An example of valid Lower Sheet mesh.

After the author tested this procedure, the obtained results were:

- Mesh and remeshing parameters definition and tuning; peculiarly, the condition posed in [19] for mesh element size must be respected.

$$\delta t \cdot \sqrt{v_f^2 + \left(\frac{v_r \cdot \pi d}{60}\right)^2} \leq \frac{1}{3} L_e \quad (12)$$

In Eq. 12, the element average size in millimeters is symbolized by L_e , dt is used for the time incremental step (obtained as total Process Time over set increments, and measured in seconds), whereas v_f and v_r are respectively feed speed in millimeters per second and screw rotational speed in rotations per minute.

- Thread forming speed correlation with feed speed and Process Time, so that to have the FE simulation set to stop at screw' head at touching the upper sheet.
- Fixing the conditions for surrounding elements; in particular *Table* was fixed, press-independent force was applied on *Blank holder*, while the *Upper sheet* was posed in simple Touching condition with the *Lower sheet*.
- Screw positioning, obtained by slightly distancing the tip surface to recover for possible lower sheet residual stresses when starting from the 2D FEA results, and to allow step-by-step deformation of the extrusions into threads; this latter was made possible by turning the screw around its vertical axis so that to have the FDS' start of threaded section hitting the workpiece' free face at first Time increment.
- "Cyclic symmetry" condition was activated to speed-up the calculations, as well as aiming the computations convergency; moreover, a peculiar solver was

employed, as indicated as best choice for 3D FE Forming simulations by the same Simufact engineers.

Apart for pursuing the right combination of all the features aforementioned, as well as the factors seen and optimized in the 2D case, the main problematic remains the huge Computational Time required for each run: a single 1% increment takes on average 81 minutes, while exploiting 4 threads on an Intel® Core® i5-6300U. The necessity to avoid extreme material deformations (Figure 49), apart from having higher computational resources available, could be completely expanding the 2D axisymmetric results into a 3D model (as suggested by the software assistance), although additionally requiring more and more Computational Time.

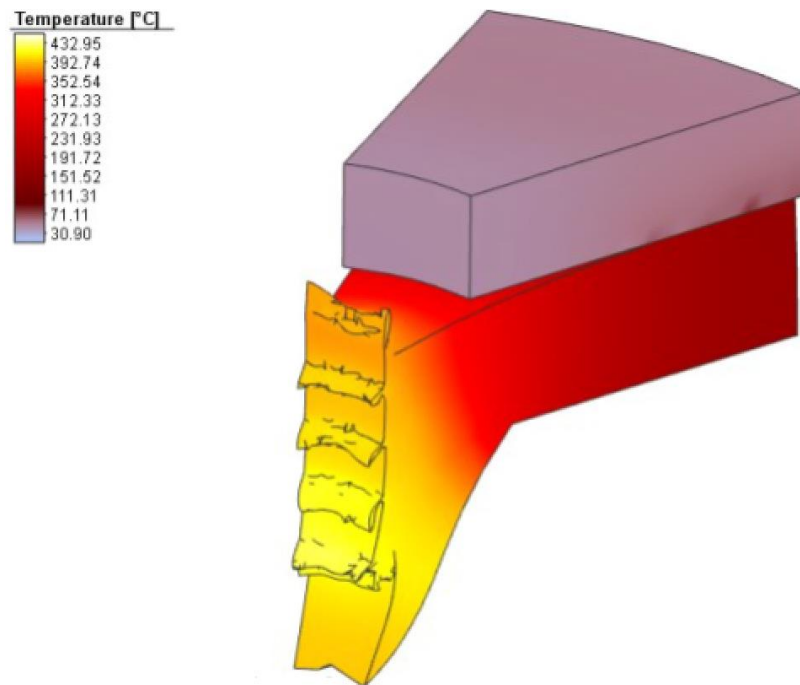


Figure 49. Thread ripping in 3D simulations.

REFERENCES

- [1] TWI® Ltd., 2021. Available: <https://www.twi-global.com/technical-knowledge/faqs/aluminium-welding/aluminium-to-steel>
- [2] Kah, Paul & Pirinen, Markku & Suoranta, Raimo & Martikainen, Jukka, “Welding of Ultra High Strength Steels. Advanced Materials Research”, 2014, Advanced Mat. Research n 849 pp 357-365, DOI: 10.4028/www.scientific.net/AMR.849.357.
- [3] Sprovieri, John, “Flow-Drilling Screws Help Carmakers Shed Weight”, February 2016, Assembly Magazine p 32.
- [4] WCL® , consulted in June 2021. Available: <https://www.wclco.com/threaded-fasteners/thread-forming-and-thread-cutting-fasteners-for-standard-panel-and-component-thickness/taptite-i-and-taptite-ii-thread-forming-screws/>
- [5] EJOT® , consulted in June 2021. Available: https://www.ejot.com/Industrial-Fasteners-Division/Products/FDS%C2%AE/p/VBT_FDS
- [6] Skovron, Jamie Daniel, "Slip-Stick Contact Conditions for the Thermo-Mechanically Coupled Flow Drill Screw Process", 2018, All Dissertations n 2185. Available: https://tigerprints.clemson.edu/all_dissertations/2185
- [7] Aslan, Fadik & Langlois, Laurent & Mangin, Philippe & Balan, Tudor, “Identification of Drilling Parameters during the Flow Drill Screw Driving Process”, 2018, Key Engineering Materials n 767 pp 465-471, DOI: 10.4028/www.scientific.net/KEM.767.465.
- [8] Pan, Xiaofei & Wu, C.T. & Hu, Wei & Wu, Y.C., “A momentum-consistent stabilization algorithm for Lagrangian particle methods in the thermo-mechanical friction drilling analysis”, 2018, Computational Mechanics n 64 pp 625-644, DOI: 10.1007/s00466-019-01673-8.
- [9] Wu, C.T. , et al., “The momentum-consistent smoothed particle Galerkin (MC-SPG) method for simulating the extreme thread forming in the flow drill screw-driving process”, 2019, Computational Particle Mechanics n 7 pp 1-15, DOI: 10.1007/s40571-019-00235-2.
- [10] Raju, B.P. & Swamy, M.K., “Finite Element Simulation of a Friction Drilling process using Deform-3D”, 2012, International Journal of Engineering Research and Applications Vol 2 Issue 6

- [11] Stéphan, Pierre & Mathurin, Florestan & Guillot, Jean, “Experimental Study of Forming and Tightening Processes with Thread Forming Screws”, 2012, Journal of Materials Processing Technology n 212 pp 766-775, DOI: 10.1016/j.jmatprotec.2011.10.029.
- [12] Weber® RSF21® presentation brochure, consulted in June 2021. Available: https://www.weber-online.com/wp-content/uploads/sites/2/RSF21_EN_1701_web.pdf
- [13] Alkelani, Ali, & Housari, Basil, “Development of Tightening Torque for Self-Tapping and Thread Rolling Fasteners”, Proceedings of the ASME 2011 Pressure Vessels and Piping Conference. Volume 2: Computer Technology and Bolted Joints. Baltimore, Maryland, USA. July 17–21, 2011. pp. 355-361, DOI: 10.1115/PVP2011-57132
- [14] Jacob, Marko, “Simulation des Temperaturfeldes und Eigenspannungen von einer MIG-Schweißung an einem Werkstück unter Berücksichtigung der temperaturabhängigen Materialeigenschaften von Aluminiumlegierungen”, 2005. DOI: 10.25643/bauhaus-universitaet.641
- [15] Yibo, Peng, et al., “Dynamic Mechanical Behaviors of 6082-T6 Aluminum Alloy”, 2013, Advances in Mechanical Engineering n 5, DOI: 10.1155/2013/878016.
- [16] SLV München, SLV Rostock, “Bericht zum Erarbeiten werkstoffkundlicher Kennwerte geschweißter Aluminiumbauteile in abhängigkeit von der Wärmeeinbringung”, 2004, DVS nr 1029. München, Abschluß-Bericht-5126.pdf
- [17] Jäckel, Mathias, et al., “Process-oriented Flow Curve Determination at Mechanical Joining”, 2020, Procedia Manufacturing n 47 pp 368-374, DOI: 10.1016/j.promfg.2020.04.289.
- [18] Kvačkaj, Tibor, et al., “Determination of ductile fracture criteria for bulk and PM materials”, 2014, Kovove Materialy n 52 pp 249-254, DOI: 10.4149/km_2014_5_249
- [19] Liu, W., et al., “Modeling and simulation of the flow drill screw process of a DP590/Al6061-T6 multi-material joint used for vehicle body”, 2020, The International Journal of Advanced Manufacturing Technology n 110 pp 1189–1201, DOI: 10.1007/s00170-020-05909-3